

Air Force Institute of Technology

AFIT Scholar

Theses and Dissertations

Student Graduate Works

3-2001

Photoluminescence of Single Quantum Well Structures in Gallium Arsenide

Christian A. Bartholomew

Follow this and additional works at: <https://scholar.afit.edu/etd>



Part of the [Optics Commons](#), and the [Semiconductor and Optical Materials Commons](#)

Recommended Citation

Bartholomew, Christian A., "Photoluminescence of Single Quantum Well Structures in Gallium Arsenide" (2001). *Theses and Dissertations*. 4565.

<https://scholar.afit.edu/etd/4565>

This Thesis is brought to you for free and open access by the Student Graduate Works at AFIT Scholar. It has been accepted for inclusion in Theses and Dissertations by an authorized administrator of AFIT Scholar. For more information, please contact richard.mansfield@afit.edu.



**PHOTOLUMINESCENCE OF SINGLE
QUANTUM WELL STRUCTURES IN
GALLIUM ARSENIDE**

THESIS

Christian A. Bartholomew, Captain, USAF

AFIT/GEO/ENP/01M-01

**DEPARTMENT OF THE AIR FORCE
AIR UNIVERSITY**

AIR FORCE INSTITUTE OF TECHNOLOGY

Wright-Patterson Air Force Base, Ohio

APPROVED FOR PUBLIC RELEASE; DISTRIBUTION UNLIMITED.

20010730 037

“The views expressed in this thesis are those of the author and do not reflect the official policy or position of the Department of Defense or the U.S. Government”

**PHOTOLUMINESCENCE OF SINGLE QUANTUM WELL STRUCTURES IN
GALLIUM ARSENIDE**

THESIS

Presented to the Faculty of the Graduate School of Engineering

of the Air Force Institute of Technology

Air University

In Partial Fulfillment of the

Requirements for the Degree of

Masters of Science in Electrical Engineering

Christian A. Bartholomew, B.S.

Captain, USAF

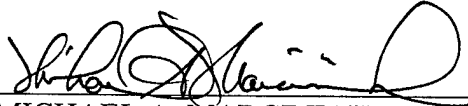
March 2001

Approved for public release; distribution unlimited

PHOTOLUMINESCENCE OF SINGLE QUANTUM WELL STRUCTURES IN
GALLIUM ARSENIDE

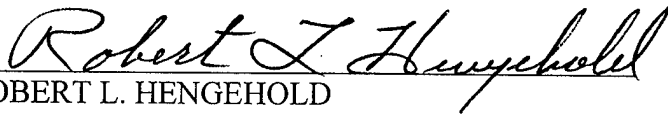
Christian A. Bartholomew, B.S.
Captain, USAF

Approved:



MICHAEL A. MARCINIAK
Assistant Professor of Physics and Deputy Head
Department of Engineering Physics
Chairman, Advisory Committee

9 Mar 01



ROBERT L. HENGEHOLD
Professor of Physics and Head
Department of Engineering Physics
Member, Advisory Committee

9 Mar '01



DAVID E. WEEKS
Associate Professor of Physics
Department of Engineering Physics
Member, Advisory Committee

9 Mar 01

PREFACE

This research, initially investigating hot-electron processes in semiconductor materials, finally took shape examining quantum well structures and laying the groundwork for future students. It has been a difficult undertaking yet one that I have definitely grown from and will look back on with great pride. It would be impossible for me to have met this challenge without the support and understanding of many people.

Providing the impetus for these experiments, I thank my advisor, Lt Col Michael Marciniak. Without his guidance and incredible patience, I never would have been able to complete this work. I also thank Dr. Robert Hengehold whose insight and immeasurable experience with semiconductors offered solutions that I may have never considered. I appreciate the models provided by Dr. David Weeks as well as his patient explanations of the difficult theory. Building and keeping this experiment in running order would have been impossible if not for Rick Patton. Without his troubleshooting prowess, I might never have had a reliable laser or an operating photon-counting scheme. I would also like to thank Rick and my lab-mate Mike McKay for their daily motivation, extraordinarily imaginative suggestions, and friendship.

I would be remiss if I did not express my appreciation to my close friends (and sympathetic AFIT-ers) for providing me with motivation to continue and enough outlets to keep me sane. Friday lunches will not be the same without the company of Dan Harvala, Bill Bernhard, Kirby Watson, Harris Hall, and Kin-Weng Chan. Finally I want to thank Jori Breemen, a confidant who may never have understood these experiments but still listened to my every frustration as she did my accomplishments.

ABSTRACT

The continued development of state-of-the-art semiconductor technologies and devices by the United States Air Force and the Department of Defense requires accurate and efficient techniques to evaluate and model these new materials. Of particular interest to the Air Force are quantum well structures which can be used for small-scale laser sources in fly-by-light applications, as efficient infrared countermeasures to heat-seeking missiles, or as advanced seekers in optically guided missiles. This thesis provides the initial experimental procedures and data necessary to begin producing accurate yet robust models. Although carrier effective masses could not be evaluated using hot-electron photoluminescence, photoluminescence excitation and temperature studies were conducted to determine the effects of strain and impurities on band structure in quantum structures. Beryllium-doped indium gallium arsenide (InGaAs:Be) quantum wells, compressively strained to lattice-match gallium arsenide, were studied, and parameters for strained energy gap, heavy hole-light hole split, and acceptor binding energy were evaluated. With the carrier effective masses fixed at accepted values, strain produced a 1.2715 eV energy gap within the well and a heavy hole-light hole split of 23.2 meV. Finally, the beryllium binding energy was found to be 22.1 meV measured above the highest valence band (first quantized heavy hole band) at 300 K.

TABLE OF CONTENTS

| | |
|---|-----|
| Preface | i |
| Abstract | ii |
| List of Figures | v |
| List of Tables..... | vi |
| List of Abbreviations and Constants | vii |
| 1. Introduction | 1 |
| 1.1. Motivation | 1 |
| 1.2. Problem Statement | 2 |
| 1.3. Organization of the Thesis | 3 |
| 2. Background and Theory | 5 |
| 2.1. Semiconductor Band Structure..... | 5 |
| 2.2. Carrier Concentrations | 10 |
| 2.3. The Fermi Level and Impurities | 16 |
| 2.4. Semiconductor Quantum Wells..... | 21 |
| 2.5. Strain in Multi-layer Structures | 27 |
| 3. Experimental Procedure | 30 |
| 3.1. Configuration..... | 31 |
| 3.2. Sample Information | 32 |
| 3.3. Execution of Experiment..... | 34 |
| 3.4. Difficulties and Lessons Learned | 38 |
| 4. Results and Discussion..... | 41 |
| 4.1. Photoluminescence Excitation | 41 |

| | |
|---|----|
| 4.2. Temperature Study | 44 |
| 4.3. Material Parameters Evaluated..... | 49 |
| 5. Conclusions and Recommendations..... | 52 |
| Appendix A: Hot-Electron Photoluminescence | 54 |
| A.1. Background..... | 54 |
| A.2. Expected Data..... | 57 |
| A.3. Observation of the Longitudinal-Optical Phonon | 59 |
| A.4. Recommendations | 61 |
| Bibliography..... | 63 |
| Vita..... | 64 |

LIST OF FIGURES

| | |
|---|----|
| Figure 2-1: Energy banding of allowed levels in diamond as a function of spacing between carbon atoms | 6 |
| Figure 2-2: Energy band diagrams of metals, insulators, and semiconductors | 7 |
| Figure 2-3: Energy-momentum band diagram showing photon absorption | 9 |
| Figure 2-4: The Fermi-Dirac distribution..... | 11 |
| Figure 2-5: The density of states function..... | 13 |
| Figure 2-6: Material carrier concentrations as determined by the Fermi-Dirac function and the density of states | 14 |
| Figure 2-7: Intrinsic, n- and p-type impurity semiconductors | 18 |
| Figure 2-8: Two-dimensional density of states function..... | 26 |
| Figure 2-9: Strain effects on valence band structure..... | 28 |
| Figure 3-1: Diagram of experimental configuration for photoluminescence studies..... | 30 |
| Figure 3-2: Theoretical energy diagram of allowed quantum levels for a 50 Å $\text{In}_{0.2}\text{Ga}_{0.8}\text{As}$ single quantum well in GaAs | 34 |
| Figure 3-3: Constant PMT voltage contours used to determine the optimal photon counting discriminator level..... | 40 |
| Figure 4-1: Photoluminescence excitation study of the InGaAs/GaAs quantum well structure | 42 |
| Figure 4-2: Photoluminescence temperature study of InGaAs/GaAs single quantum well..... | 45 |
| Figure 4-3: Temperature dependence of transition energy | 48 |
| Figure A-1: Energy diagram of hot electron recombinations | 58 |
| Figure A-2: Observed longitudinal-optical phonon replicas of the laser excitation line | 60 |

LIST OF TABLES

| | |
|---|----|
| Table 2-1: Effects of material effective masses and the introduction of impurity atoms on the Fermi level | 19 |
| Table 3-1: Material constants for GaAs, InAs, and strained $\text{In}_{0.2}\text{Ga}_{0.8}\text{As}$ | 33 |
| Table 4-1: Varshni α and β coefficients fit to the data in Fig. 4-3 | 48 |
| Table 4-2: Summary of material constants evaluated in this thesis | 51 |

LIST OF ABBREVIATIONS AND CONSTANTS

| | |
|-----------|---|
| Å | Angstrom, a unit of length equal to 10^{-10} meters |
| eV | Electron volt, a unit of energy equal to $1.602\ 177\ 33 \times 10^{-19}$ Joules |
| GaAs | Gallium arsenide |
| h | Plank's constant, $6.626\ 075\ 5 \times 10^{-34}$ J·s |
| \hbar | Dirac's constant equal to $h/2\pi$ |
| InGaAs:Be | Beryllium-doped indium gallium arsenide |
| J | Joules, a unit of energy equal to $1\ \text{kg}\cdot\text{m}^2\cdot\text{s}^{-2}$ |
| k | Boltzmann's constant, $1.380\ 658 \times 10^{-23}$ J·K ⁻¹ |
| K | Kelvin, a measure of thermodynamic temperature |
| LO | Longitudinal optical |
| m_0 | Electron rest mass, $9.109\ 389\ 7 \times 10^{-31}$ kg |
| MBE | Molecular-beam epitaxy |
| meV | Milli-electron volts |
| mW | Milliwatts |
| nm | Nanometers |
| PLE | Photoluminescence excitation |
| PMT | Photomultiplier tube |
| SNR | Signal-to-noise ratio |
| SQW | Single quantum well |
| μm | Microns or micrometers |

1. Introduction

1.1. Motivation

The continued development of state-of-the-art semiconductor technologies and devices by the United States Air Force and the Department of Defense requires accurate and efficient techniques to evaluate and model these new materials. As new, and more complicated, semiconductor structures emerge, the defense scientific community, mainly the Air Force Research Laboratory, not only needs indigenous methods of experimentally measuring the photoelectric characteristics of the structure, but also suitable modeling techniques and parameters. These models allow initial analysis of new materials without time-consuming experimental investigation, which may later be performed at length on appropriate candidates.

Of particular interest to the Air Force are quantum structures, including quantum wells and dots, which can be used for small-scale laser sources in fly-by-light applications, as efficient infrared countermeasures to heat-seeking missiles, or as advanced seekers in optically guided missiles. As the successor to fly-by-wire, fly-by-light technology aspires to replace conventional current-carrying wire with optical fibers to receive pilot commands and actuate the appropriate flight control surface. This upgrade offers the ability to carry multiple signals (through wavelength multiplexing) over the same line; however, this lightweight, highly reliable, and electromagnetically immune aircraft flight control system is dependent on semiconductor photodetectors and emitters. Mid-infrared quantum well lasers are also suited to deliver high power over narrow spectral ranges to spoof the guidance algorithm or even destroy the detector of

heat-seeking missiles. On the other hand, similar devices could also be employed as detectors in friendly heat-seeking missiles. In all of these proposed applications, the efficiency and relatively small size of these devices is paramount to integration in aircraft or missiles where space and weight are at a premium.

As the technology for growing thin layers of semiconductor materials and creating quantum structures continues to improve, intricate models must be developed for initial analysis of these structures' utility for the above-mentioned military applications. These models, however, are dependent on many parameters including dopant or impurity concentrations, strain induced by forcing different materials to be grown together, and simple quantities such as material composition and well dimensions. This thesis will determine these quantities for simple quantum wells at zone center and compose the methodology for expanding semiconductor modeling beyond zone center.

1.2. Problem Statement

Although many semiconductors have been intensely investigated for use as lasers and detectors, most work concentrated on zone center phenomena without considering band structures further out in momentum space. One such method of validating current band models is through hot-electron spectroscopy, observing the higher energy transitions of electrons away from zone center. Beginning with a well-known material such as gallium arsenide, data from hot-electron photoluminescence (PL) can be analyzed and compared to that of previous hot-electron experiments. Similar experiments can then be performed on new semiconductor materials or heterostructures. Together with

experiments concerning nonradiative processes, both the structure and efficiency of the semiconductor material can be established.

This modeling effort must also address the complexities introduced by strain in heterostructures and by the introduction of impurities. Sufficient experimental data must be collected for characterization and determination of parameter significance in order to validate a computational model. Single quantum well structures in gallium arsenide provide an excellent origin for initial analysis and verification of a proposed model since there has been abundant research and previous experimentation which may be used for comparison.

Although hot-electron photoluminescence is the ultimate goal of this research, it is necessary to begin with simple photoluminescence studies to verify basic material parameters as well as optimal configuration of the experiment. For this initial work, simple zone-center, one-dimensional, finite-depth, quantum-well solutions to Schrodinger's wave equations can be easily reached which are in close agreement with more complicated models used in the hot-electron region. Once this first step is complete, hot-electron photoluminescence studies can be completed and more complete models, and their associated parameters, can be proposed for beyond zone center, as well.

1.3. Organization of the Thesis

The thesis is divided into five chapters and one appendix. After this introduction, a background of semiconductor theory and relevant quantum physics are covered in Chapter 2. Chapter 3 outlines the experimental procedures and setup used for collection of photoluminescence data, which is analyzed and characterized according to the

postulated models in Chapter 4. Finally, Chapter 5 concludes the thesis with overall observations and recommendations for future study. An appendix addresses the original scope of this thesis, including relevant experiments performed by others, significant observations, and suggestions for completion of the hot-electron photoluminescence experiment.

2. Background and Theory

Beginning with an explanation of the band structure resulting from the atomic arrangement of the material, a review of the theory associated with semiconductor materials is presented in this chapter. Determination of the concentrations of carriers, electrons and holes, in these bands will be addressed as well as the impact of introducing impurities into the structure. Finally, the above topics will be applied to quantum well structures and the effects of strain caused by forced lattice matching at the well interfaces will be covered.

2.1. Semiconductor Band Structure

As an individual atom whose electrons occupy bound orbits begins to interact with another atom, a band of allowed energies forms, replacing the discrete energies of the isolated atom. If N similar atoms are brought together, their electron wave functions begin to overlap and from the Pauli exclusion principle with two possible spin states for each electron, $2N$ electrons of the same original orbital of the individual atoms now occupy $2N$ slightly different states of the multi-atom crystal (8: 1). The distribution of these different states is dependent upon the interatomic distance of the crystal, which is demonstrated in Fig. 2-1 for individual carbon atoms forming a diamond crystal. As this banding occurs, energetically separated bands, as shown for diamond, are created. In the case of a semiconductor, the highest energy band that is completely filled with electrons at absolute zero is referred to as the valence band. The next higher energy band is completely empty at absolute zero and is referred to as the conduction band.

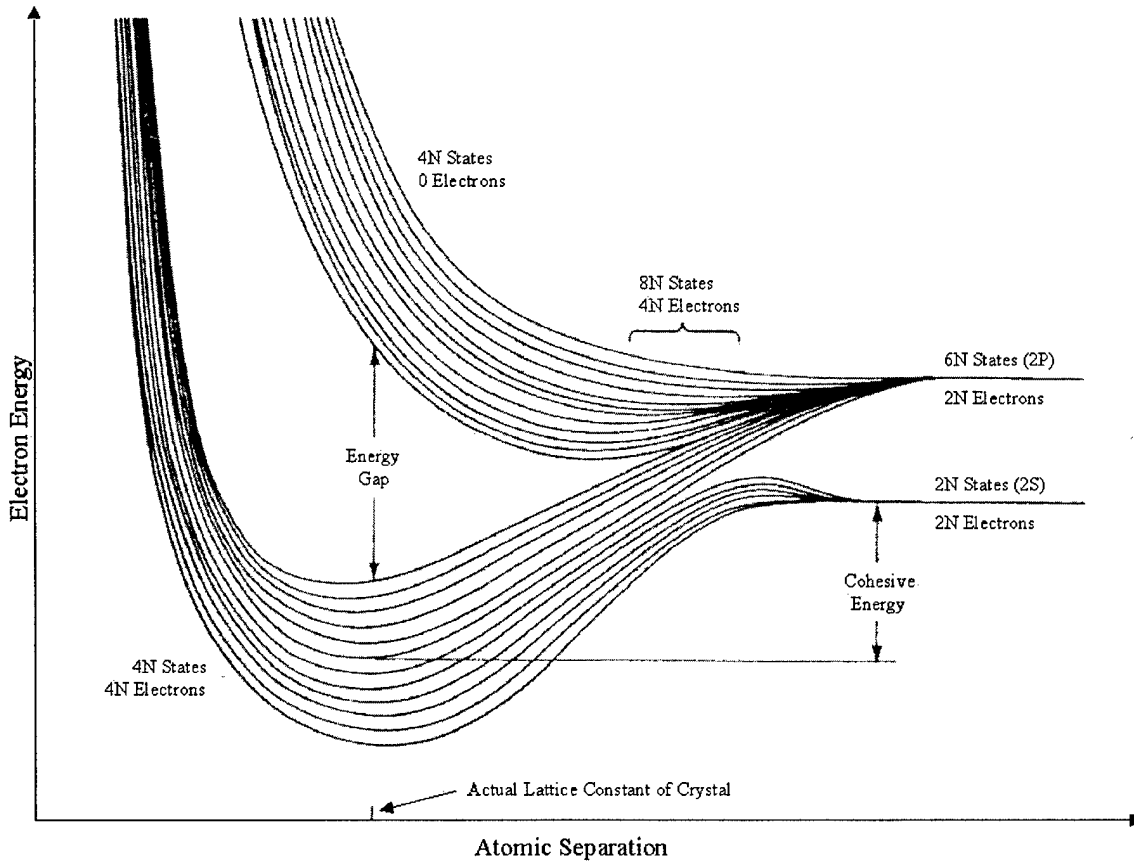


Fig. 2-1. Energy banding of allowed levels in diamond as a function of spacing between carbon atoms. As interatomic distances decrease, interaction between electron wave functions cause discrete orbitals to split into conduction and valence energy bands. (4: 560)

The banding of energy levels as atoms interact applies to all atoms as they form solids and allows for their categorization by conduction and valence band structure. Conductors are classified by a partially filled energy band, even at absolute zero, or by an overlapping conduction and valence band. This allows electrons to easily traverse the solid thereby conducting current. Insulators, like semiconductors, have no electrons in their conduction band and, furthermore, have a large energy gap between the conduction and valence bands. This gap prevents electrons from being thermally excited into the conduction band, thus preventing current flow through the solid. Semiconductors are intrinsic insulators but with a narrower energy gap. This allows semiconductors to act as

conductors if electrons are excited into the conduction band, which can easily be accomplished at relatively low temperatures or through photon interaction. Fig. 2-2 shows the distinction between conductors, insulators, and semiconductors.

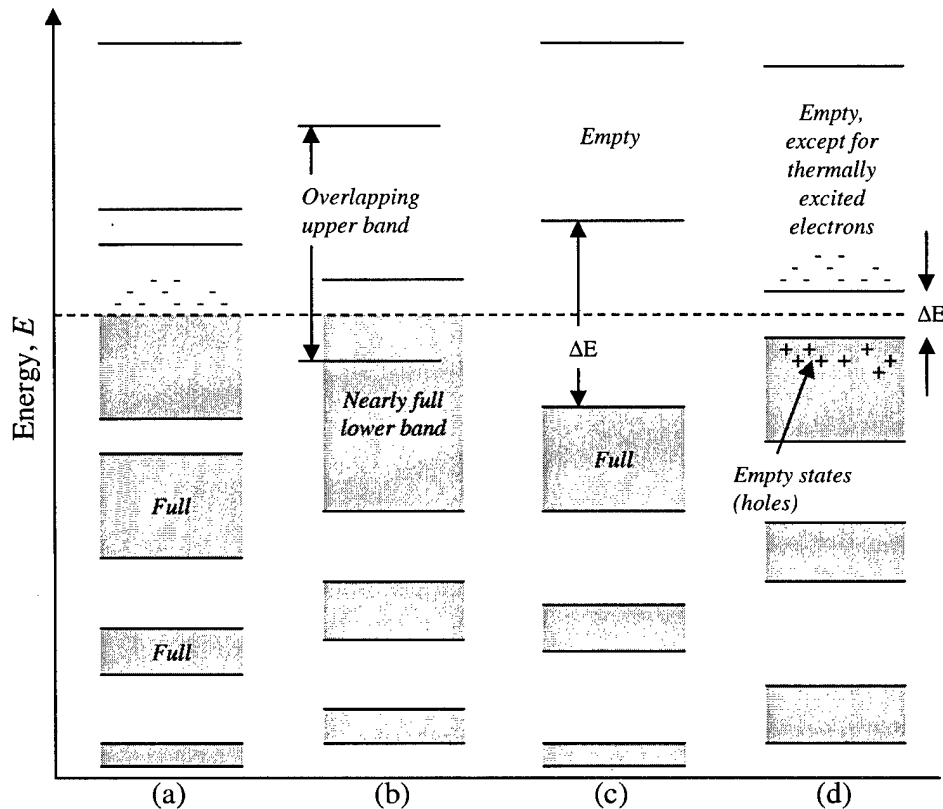


Fig. 2-2. Energy band diagrams of (a) metals having a partially filled band, (b) metals with overlapping bands, (c) insulators, and (d) semiconductors. Shaded regions are completely full of electrons at absolute zero. Conductors are characterized by having free electrons in the conduction band while insulators have completely empty conduction bands. Semiconductors have smaller energy gaps than insulators and therefore may have thermally excited electrons above absolute zero. (7: 362)

The thermal excitation of valence electrons to the conduction band in semiconductors is described as a probability given by the Fermi-Dirac distribution which is discussed in the next section. Valence electrons may also be excited through the absorption of a photon with energy greater than the semiconductor energy gap, E_g . The

photon energy is $h\nu$, where h is Planck's constant and ν the frequency of the incident light. This seems an obvious consequence of the energy band structure shown in Fig. 2-2, however these bands are much more complicated and electron (and photon) momentum must also be considered.

The kinetic energy of an electron is related to its velocity through the classical physical relation

$$E = \frac{1}{2} m_c^* v^2 \quad [2.1-1]$$

while its momentum is described by

$$p = m_c^* v \quad [2.1-2]$$

where m_c^* is the effective mass of the electron in the material and v is its velocity. In quantum mechanics, the particle momentum, p , is related to the wave vector, k , by

$$p = \hbar k \quad [2.1-3]$$

where \hbar is Dirac's constant, with $\hbar = h/2\pi$. Combining the above equations, the electron energy can be related to the wave vector, now more appropriately called the momentum vector, as

$$E = \frac{\hbar^2 k^2}{2m_c^*} \quad [2.1-4]$$

A similar relation can be written for the empty states, or holes, in the valence band using the hole effective mass. Now the band structure of a simple semiconductor material can be modeled and transitions of valence band electrons to the conduction band through photon absorption can be evaluated. Since photons are purely energetic particles with negligible momentum, they elicit no momentum change in the electron excited. In an

energy-momentum band diagram, this is represented as a vertical transition of the electron (Fig. 2-3).

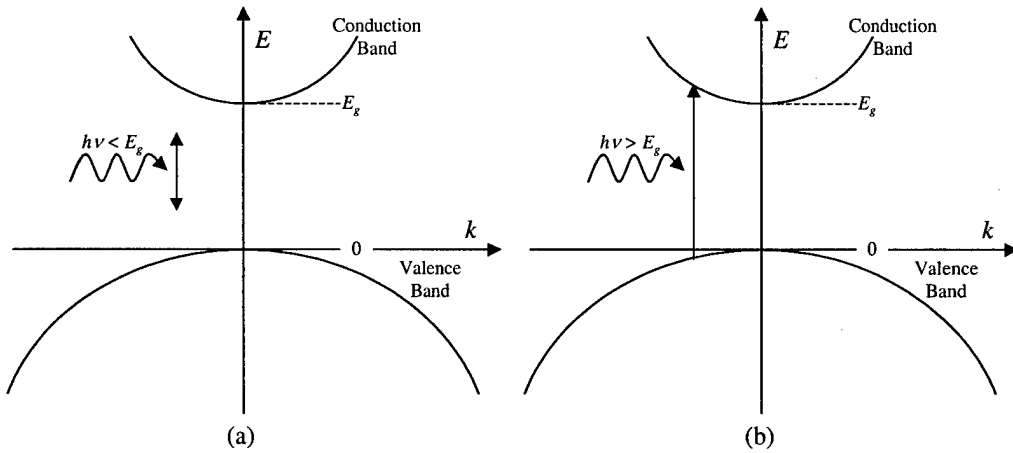


Fig. 2-3. Energy-momentum band diagram showing photon absorption. If the photon is not of sufficient energy (a), it is not absorbed and the material is transparent to that wavelength. At energies higher than the bandgap (b), the photon may be absorbed if there is an available electron and corresponding hole directly above it.

Just as photons can be absorbed by the semiconductor, exciting a valence electron into the conduction band, an electron already in the conduction band may transition back to the valence band by giving up a photon. This may occur at any electron position in the $E-k$ parabolic band, so long as a hole exists directly below in the valence band such that momentum is conserved. The electron can also nonradiatively relax to the conduction band minimum at $k = 0$ through the emission of phonons. Once at zone center, the electron will relax to the valence band and a photon is emitted. The photon creation process is called spontaneous emission and its rate, $r_{sp}(\nu)$, will be determined at the end of the next section. The radiative recombination lifetime, a material constant τ_r , will help calculate this rate which determines the number of photons emitted in a specific frequency (wavelength) range. Thus, as stated above, it is possible for electrons at any position in the band to recombine. However, it will be shown that this becomes less

probable for electrons further away from zone center due to the concentrations of electrons and available holes.

2.2. Carrier Concentrations

In a semiconductor material at absolute zero, there are no electrons in the conduction band and no empty states, or holes, in the valence band. Without free charged particles, or carriers, the semiconductor is nothing but an insulator. Although electrons could be introduced into the conduction band through the absorption of light, electrons also have the ability to be thermally excited into the conduction band as temperature increases above zero. This leaves behind a hole and with this set of carriers, the semiconductor begins to allow current conduction.

The distribution in energy of electrons in a semiconductor in thermal equilibrium at temperature T is given by the Fermi-Dirac distribution,

$$f_c(E) = \frac{1}{1 + e^{(E-E_F)/kT}} \quad [2.2-1]$$

where k is Boltzmann's constant and E_F is defined as the Fermi level, the energy at which the probability of finding an electron is $1/2$ (8: 7). In the most simplistic model, the Fermi level is in the middle of the energy gap (i.e., halfway between the conduction and the valence bands) as shown in Fig. 2-4. Note that only at absolute zero, when the distribution is a step function, is the probability of an electron in the conduction band exactly zero.

The distribution of holes in the valence band is directly related to that of electrons in the conduction band since the hole was created by the excitation of the electron. The exact equation is

$$f_v(E) = 1 - f_c(E) = \frac{e^{(E-E_F)/kT}}{1 + e^{(E-E_F)/kT}} = \frac{1}{1 + e^{-(E-E_F)/kT}} \quad [2.2-2]$$

This is only the first step in determining the overall carrier concentration since this distribution predicts electrons within the energy gap, which is not possible. Therefore, it is necessary to develop another function which predicts the number of allowed energies.

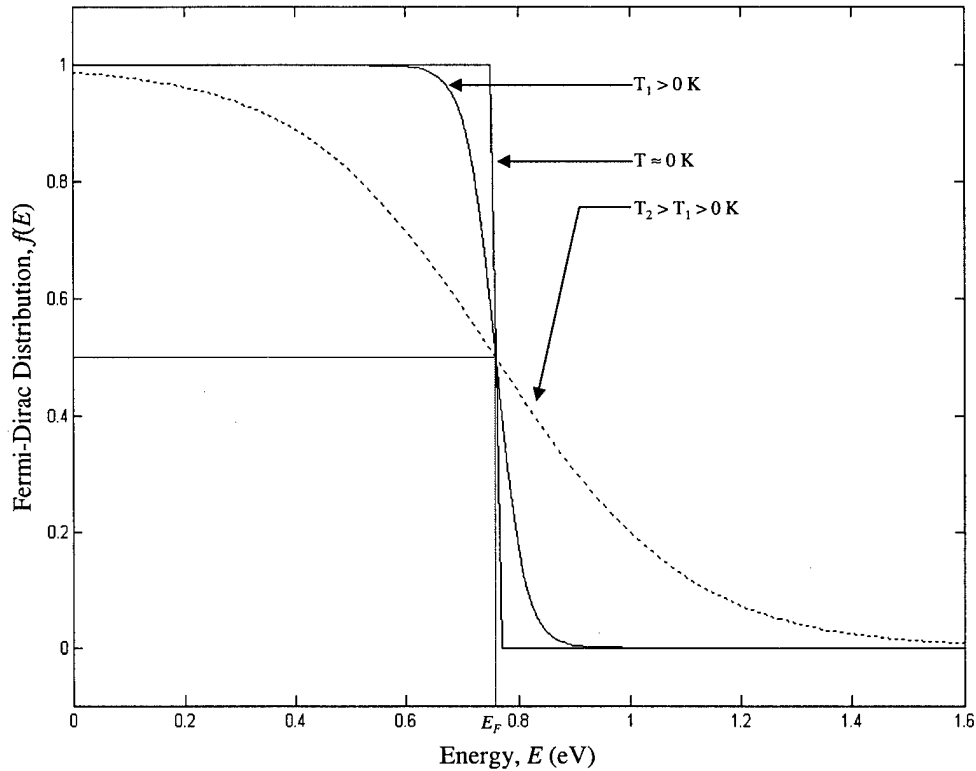


Fig. 2-4. The Fermi-Dirac distribution. The distribution changes from a step function at absolute zero, where the probability of finding an electron in the conduction band is exactly zero, to a smoother function whose tails extend electron energy probability into the conduction band at higher temperatures.

To find a density of allowed states, it is first necessary to find the volume of phase space between two energy surfaces at E and $E + dE$. The allowed energy states are uniformly distributed in phase space and therefore in momentum (k -) space. A single state occupies a volume of $8\pi^2/V$ in momentum space, where V is the real space crystal

volume. Incorporating two possible spins for each electron, the number of states in the interval E and $E + dE$ is (7: 352)

$$g(E)dE = \frac{4\pi}{h^3} (2m^*)^{3/2} E^{1/2} dE \quad [2.2-3]$$

However, the energy, E , must be measured with respect to the edge of the energy band.

Thus, this equation becomes

$$g_c(E) = \frac{4\pi}{h^3} (2m_c^*)^{3/2} (E - E_c)^{1/2} \quad [2.2-4]$$

for electrons in the conduction band (Fig. 2-5). A similar equation represents the number of allowed states for holes in the valence band by measuring E from the top of the valence band (normally set to zero by convention) and using the hole effective mass. Since both functions are not defined for energy values within the semiconductor energy gap, the density of states is set to zero since there are no allowed energy levels present within the energy gap. Together with the Fermi-Dirac distributions, the density of states functions define the carrier concentrations within the material.

Combining the Fermi-Dirac distribution of electrons with the electron density of states function for the conduction band, the total number of thermally excited electrons at each energy level in the conduction band can be determined by

$$N_c(E) = f_c(E) \cdot g_c(E) = \frac{4\pi}{h^3} (2m_c^*)^{3/2} (E - E_c)^{1/2} (1 + e^{(E-E_F)/kT})^{-1} \quad [2.2-5]$$

A similar function can be developed for holes in the valence band and both are diagrammed in Fig. 2-6. Note that the maximum electron (hole) population does not occur at the conduction (valence) band minimum (maximum). As material temperature increases, more electrons can be thermally excited higher into the conduction band. Even

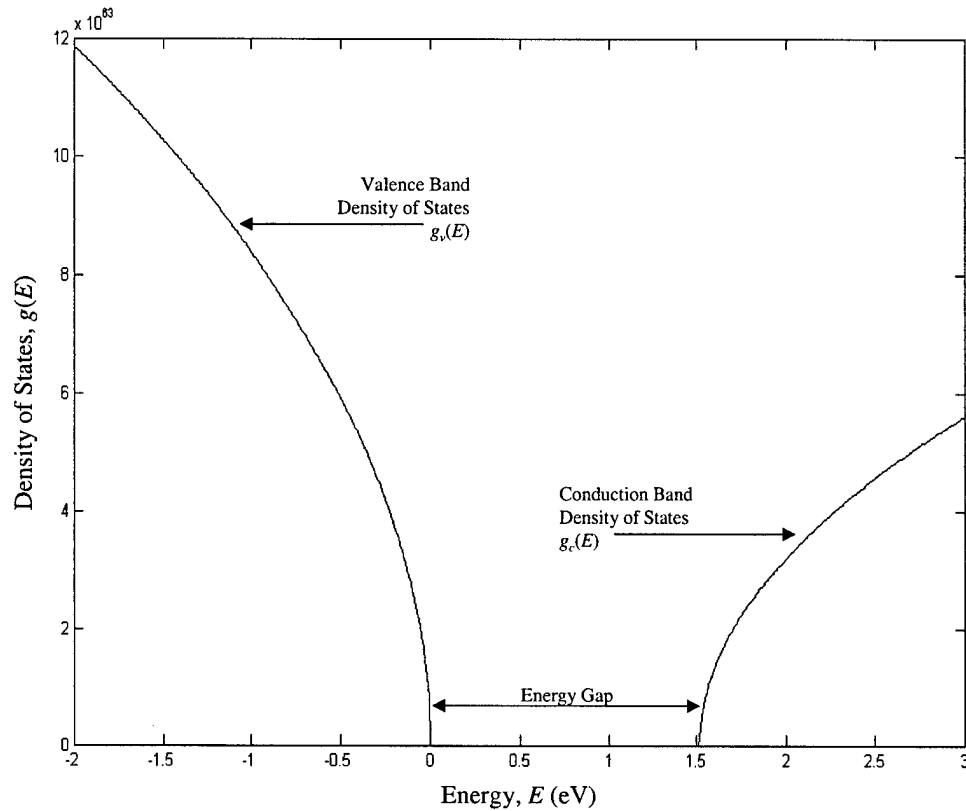


Fig. 2-5. The density of states function. The conduction band density of states describes the number of allowed energy states for electrons and therefore relies on the electron effective mass in the material. With a (normally) higher effective mass for holes in the valence band, its density of states function is much wider than that of the conduction band. Within the semiconductor energy gap there are no allowed states, thus both functions are precisely zero.

as the occupancy probability tails off as energy increases into the conduction band, with more states at these higher energies than at the conduction band minimum, the overall electron concentration reaches a maximum further into the band. Although this is not precisely the case for photoluminescence (PL) studies since the semiconductor is in electrical but not necessarily thermal equilibrium, the overall concept can be expanded to address PL. The energies of the maximum electron and hole concentrations in their respective bands will establish the peak photon emission wavelength, while the relative

shapes of these concentrations will dictate the width and lineshape of the emission profile.

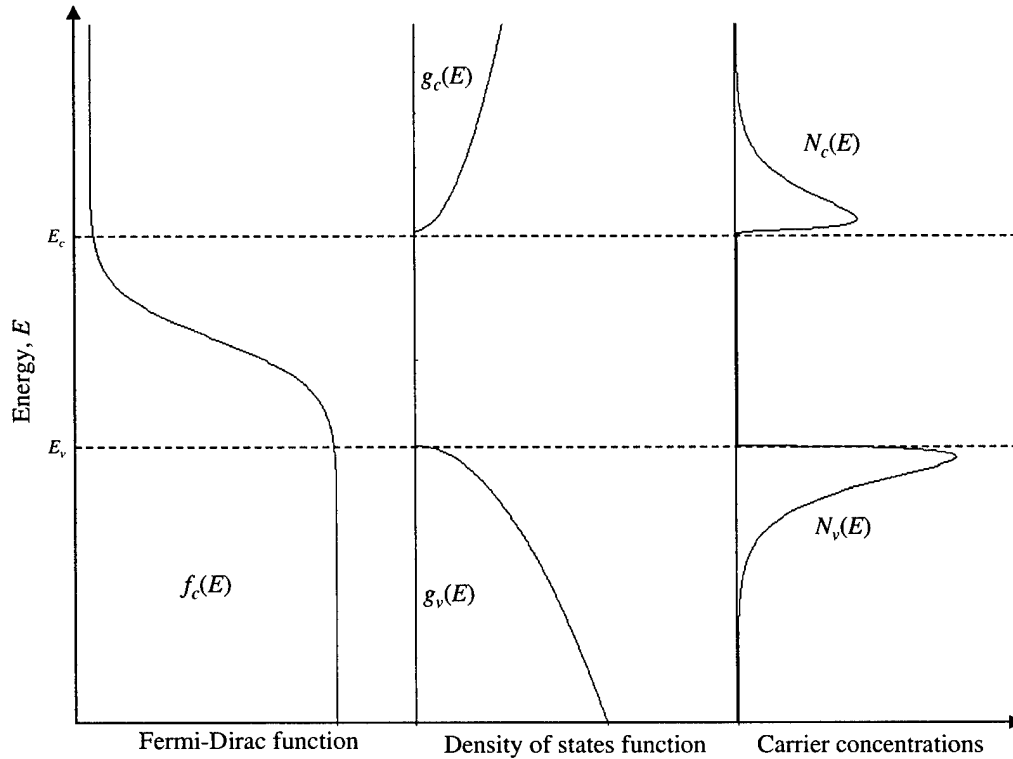


Fig. 2-6. Material carrier concentrations as determined by the Fermi-Dirac function and the density of states. The lower effective mass of the electron as compared to that of the hole accounts for the difference in carrier concentration shapes given a mid-gap Fermi level.

As mentioned previously, the spontaneous emission rate is a function of wavelength, since it depends on the number of carriers at each allowed energy state, as well as their lifetime for occupying that state. To determine this rate, first consider a semiconductor in thermal equilibrium. Thus, the Fermi-Dirac distribution for electrons in the conduction band is symmetric to the distribution of holes in the valence band about the Fermi level, or

$$f_c(E + E_F) = f_v(E_F - E) \quad [2.2-6]$$

If the Fermi level is within the energy gap and away from the conduction and valence band edges, the Boltzmann distribution approximates the Fermi-Dirac distribution as

$$f_c(E) = \frac{1}{1 + e^{(E-E_F)/kT}} \approx e^{-(E-E_F)/kT} \quad [2.2-7]$$

It now becomes necessary to define a new distribution function that considers distributions in both the conduction and valence band suitable for spontaneous emission. This emission distribution is therefore dependent not on a specific energy but on an energy difference and can be written as a function of the frequency of a photon emission due to an electron transition through that energy difference

$$f_e(\nu) = f_e\left(\frac{E_2 - E_1}{h}\right) = f_c(E_2) \cdot f_v(E_1) = f(E_2) \cdot [1 - f(E_1)] \quad [2.2-8]$$

After applying the Boltzmann approximation, this becomes

$$f_e(\nu) \approx e^{-(E_2-E_F)/kT} \cdot e^{-(E_F-E_1)/kT} = e^{-(E_2-E_1)/kT} = e^{-h\nu/kT} \quad [2.2-9]$$

which no longer has a Fermi energy dependence. Again, this emission distribution only describes the likelihood of transitions at a given frequency without considering the actual density of allowed transition energies.

Depending on both the conduction and valence density of states functions, this density of allowed transitions is called the “joint density of states function,” and is developed from [2.2-3]. For this joint density of states, the energy of the spontaneously emitted photons is measured with respect to the energy gap, and the material mass of the entire system is used. Thus, [2.2-3] becomes

$$g(E) = \frac{4\pi}{h^3} (2m_r^*)^{3/2} (h\nu - E_g)^{1/2} \quad [2.2-10]$$

for a joint density of states, where $h\nu$ is the photon energy (based on its frequency, ν) and m_r^* is the reduced mass of electrons and holes given by

$$\frac{1}{m_r^*} = \frac{1}{m_c^*} + \frac{1}{m_v^*} \quad [2.2-11]$$

By multiplying the Fermi distribution with the joint density of states function and then dividing by the radiative recombination lifetime, the spontaneous emission rate as a function of frequency is found as

$$r_{sp}(\nu) = \frac{1}{\tau_r} g(\nu) f_e(\nu) = \frac{4\pi(2m_r^*)^{3/2}}{h^2\tau_r} (h\nu - E_g)^{1/2} e^{-h\nu/kT} \quad [2.2-12]$$

The peak of this spontaneous emission will occur at the maximum of the rate in [2.2-12], which is determined by setting its derivative to zero, and is given by

$$\nu_p = \frac{E_g + \frac{kT}{2}}{h} \quad [2.2-13]$$

This equation for the peak frequency is not entirely correct since the Boltzmann approximation was used to make evaluation of the Fermi-Dirac distribution simpler. Although valid if the Fermi level is within the energy gap and sufficiently far from either band, this approximation begins to break down when impurities or dopants are introduced and the Fermi level is shifted closer to one of the bands.

2.3. The Fermi Level and Impurities

Since the carrier distribution is dependent upon the Fermi level, it is important to determine an accurate approach to finding it in various semiconductor materials. Although a simplistic model places the Fermi level at the middle of the energy gap, this is obviously incorrect from Fig. 2-6, which showed that the number of holes in the valence

band exceeds the number of electrons in the conduction band. This is impossible—a hole is created by the absence of an electron, so the number of holes must equal the number of electrons. The relative difference in carrier concentrations shown in Fig. 2-6 is caused by the difference in the effective masses of holes and electrons used to calculate the density of states. Therefore, a correction factor based on these effective masses must be introduced in the establishment of the Fermi level. The total concentration of thermally excited electrons in the conduction band is calculated by integrating $N_c(E)$ from [2.2-5] over all energies yielding

$$n_0 = 2 \left(\frac{2\pi m_c^* kT}{h^2} \right)^{3/2} e^{-(E_c - E_F)/kT} \quad [2.3-1]$$

A similar equation can be found for the total number of holes in the valence band, p_0 , however relying on the hole effective mass and the energy position of the valence, not conduction, band. After equating these two functions to find the intrinsic carrier concentration, the Fermi energy can also be solved for as

$$E_F = \frac{1}{2}(E_c - E_v) + \frac{3}{4}kT \ln \frac{m_v^*}{m_c^*} = \frac{E_g}{2} + \frac{3}{4}kT \ln \frac{m_v^*}{m_c^*} \quad [2.3-2]$$

which corrects for the effective mass difference between holes and electrons in most semiconductor materials (7: 390).

This rectifies the apparent error in Fig. 2-6 by shifting the Fermi level slightly higher, evening out the area under the curves and equating the number of holes in the valence band to the number of electrons in the conduction band; however, this applies only to intrinsic semiconductors. With the introduction of impurities (called dopants when their introduction is intentional), the electron and hole populations depend on the number of impurities as well as the number of intrinsic carriers from [2.2-5]. By

substituting atoms with one more valence electron, such as group V atoms onto the group V sites in a III-V semiconductor or group V atoms into an group IV semiconductor, a positive ion is introduced into the lattice, contributing the extra electron which cannot covalently bond. This type of substitution is referred to as introducing donor atoms since they easily donate conduction electrons to the material. This is shown in Fig. 2-7, where phosphorus (group V) atoms are added to a silicon (group IV) semiconductor to provide donor atoms and excess electrons. This is called n-doping since these extra electrons cause conduction by a negative charge carrier. Similarly, the introduction of atoms with one less valence electron adds a negative ion to the lattice and a missing covalent bond, or hole. Adding boron (group III) atoms to the silicon structure

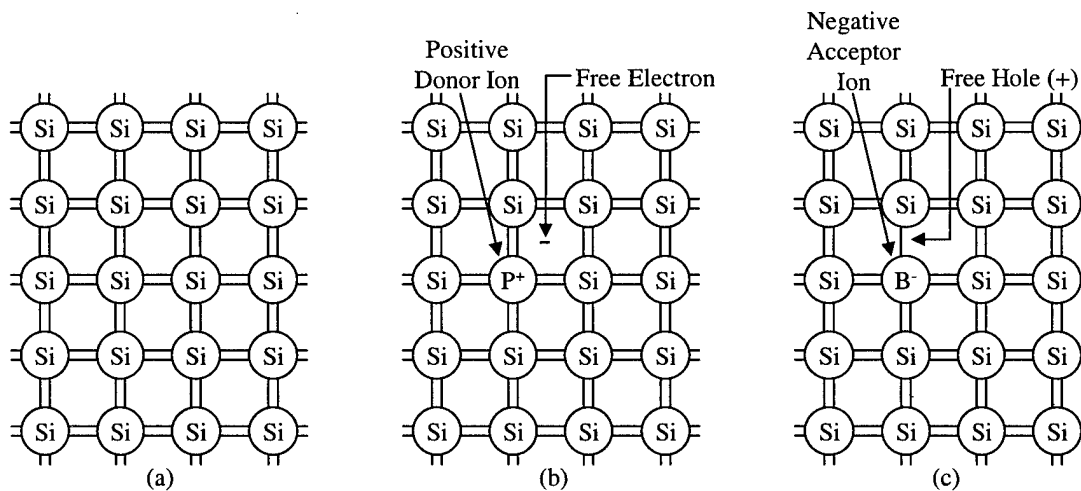


Fig. 2-7. Intrinsic, n- and p-type impurity semiconductors. The introduction of impurity atoms into the intrinsic silicon semiconductor (a) create impurity semiconductors. The phosphorous impurity atom contributes an extra electron which cannot covalently bond forming an n-type semiconductor (b). The net negative charge introduced by the electron is balanced by the positive donor ion. The p-type impurity semiconductor (c) balances the free hole with a negative (boron) acceptor ion.

p-dopes the material with acceptor ions and excess holes, causing conduction by a positive charge carrier.

As discussed earlier for intrinsic semiconductors, the equilibrium electron and hole concentrations must be equal; however, this is not necessarily true in impurity semiconductors. The overall charge neutrality of the crystal provides the only restriction such that the number of free electrons and holes must be balanced by positive and negative ions in the lattice. From this, the new Fermi level can be found as (7: 391)

$$E_F = E_{Fi} + kT \sinh^{-1} \left(\frac{N_d - N_a}{2n_i} \right) = \frac{E_g}{2} + \frac{3}{4} kT \ln \frac{m_v^*}{m_c^*} + kT \sinh^{-1} \left(\frac{N_d - N_a}{2n_i} \right) \quad [2.3-3]$$

where N_d and N_a are the number of donor and acceptor ions in the material and n_i is the intrinsic carrier concentration of the material. Thus, the presence of impurities in semiconductors shifts the Fermi level, which in turn shifts the carrier distribution functions and the overall carrier concentrations. This can be seen in Table 2-1 where $N_a = 5 \times 10^{17} \text{ cm}^{-3}$ beryllium atoms are substitutionally added to gallium arsenide.

Table 2-1. Effects of material effective masses and the introduction of impurity atoms on the Fermi level. The mid-gap approximation is adjusted due to the effective masses of holes ($m_v^* = 0.51m_0$) and electrons ($m_c^* = 0.067m_0$) in gallium arsenide to determine the intrinsic Fermi level. Finally, $N_a = 5 \times 10^{17} \text{ cm}^{-3}$ beryllium atoms are introduced and the resulting shift in the Fermi level calculated. Unless otherwise noted, all levels are for room temperature, $T = 300 \text{ K}$. All energies are measured from the top of the valence band.

| Description | Energy (eV) |
|---|-------------|
| Direct Bandgap, E_g | 1.519 |
| Midgap Fermi Level Approximation | 0.759 |
| Intrinsic Fermi Level | 0.799 |
| Extrinsic Fermi Level | 0.0930 |
| Extrinsic Fermi Level at Low Temperatures (7 K) | 0.0092 |

This final equation for the Fermi level is appropriate only if the semiconductor is in thermal equilibrium. Although this is normally the case, there are situations where an external electric current or an incident photon flux could cause a state of quasi-equilibrium. In this case, the electrons in the conduction band are in thermal equilibrium with themselves and the holes in the valence band are also in equilibrium; however, no mutual thermal equilibrium between them exists. In these circumstances, two quasi-Fermi levels are developed, a one for the conduction band and an independent one for the valence band. Since these levels can lie within the conduction or valence bands, the resulting carrier concentrations found after multiplication by the density of states can be quite large (11: 558).

The presence of impurities in semiconductors not only shifts the Fermi levels, creating disparate carrier concentrations within the bands, but also produces allowed energies within the energy gap for carriers to occupy. P-type impurities create an acceptor energy level above the valence band maximum, while n-type impurities create a donor level below the conduction band minimum. The distance (in energy) from the respective bands is the ionization energy of the impurity in the semiconductor, is constant with respect to k in momentum space, and is normally less than 100 meV (8: 9). With another allowed level for carriers to occupy, transitions may also occur between bands and impurities. These impurity-to-band transitions can occur from a donor level to the valence band or from the conduction band to an acceptor level, producing a photon with energy below that of the energy gap. For these transitions to occur, the impurity levels must be partly deionized such that the holes of the acceptor atoms are not thermally populated by electrons or, likewise, the electrons attached to the donor atoms are not all

thermally excited into the conduction band. This is normally true at sufficiently low temperatures, moving the Fermi level to an energy between the impurity energy and the band edge. At these low temperatures, the Fermi level for an extrinsic semiconductor doped with N_a acceptors becomes

$$E_F = \frac{E_A}{2} - \frac{1}{2}kT \ln \frac{N_a h^3}{4(2\pi m_v^* kT)^{3/2}} + kT \sinh^{-1} \left(\frac{(2\pi m_v^* kT)^{3/4} e^{-E_A/kT}}{2h^{3/2} N_a} \right) \quad [2.3-4]$$

where E_A is the acceptor binding energy.

2.4. Semiconductor Quantum Wells

The development thus far was concerned with semiconductor materials of sufficient volume that electrons and holes within the energy bands did not encounter quantum mechanical constraints. If the size of the semiconductor is comparable to or smaller than the deBroglie wavelength of thermalized electrons, quantum effects within the allowed energy bands must be considered (11: 569). It is therefore necessary to examine carriers confined within this small-scale potential energy structure only as waves and not particles. To do so through quantum mechanics, the behavior of an electron or hole is described by the wavefunction $\psi(x, y, z, t)$, which is the solution to the Schrödinger wave equation

$$\left[-\frac{\hbar^2}{2m} \nabla^2 + V(x, y, z, t) \right] \psi = i\hbar \frac{\partial \psi}{\partial t} \quad [2.4-1]$$

where $V(x, y, z, t)$ is the potential energy function of the particle and ∇^2 is the Laplacian operator given by

$$\nabla^2 = \frac{\partial^2}{\partial x^2} + \frac{\partial^2}{\partial y^2} + \frac{\partial^2}{\partial z^2} \quad [2.4-2]$$

For a semiconductor in electronic equilibrium, the potential function becomes time-independent and the Schrödinger equation can be separated by letting

$\psi(x, y, z, t) = u(x, y, z)g(t)$ giving

$$-\frac{\hbar^2}{2m}\nabla^2 u + Vu = Eu \quad [2.4-3]$$

where E is the separation constant (with respect to position) given by

$$E = \frac{i\hbar}{g(t)} \frac{dg(t)}{dt} \quad [2.4-4]$$

More importantly, E is the energy eigenvalue of the system corresponding to the expectation value of the system's total energy (15: 9).

A quantum well is a double heterojunction structure consisting of an ultrathin layer of material whose energy gap is smaller than the material surrounding it. The ultrathin region creates rectangular potential wells in the conduction and valence bands set by the surrounding materials. Electrons and holes can become confined within these wells, however only at discrete energy levels due to distinct solutions to the Schrödinger equation. For any quantum well, the time-independent Schrödinger equation further simplifies to a one-dimensional equation in x since the structure is assumed to extend sufficiently in the y - and z -directions to forego quantum analysis. The quantized energy eigenvalues in the case of the infinitely deep well are

$$E^q = \frac{h^2 q^2}{8md^2}, \quad q = 1, 2, 3, \dots \quad [2.4-5]$$

where d is the well width and m is the mass of the confined particle (11: 570). For application to a conduction band finite potential well, this energy is the separation

between the q th allowed electron energy state and the conduction band minimum such that

$$E = E_c + E_c^q = E_c + \frac{\hbar^2 q^2}{8m_c^* d^2} \quad [2.4-6]$$

This infinite potential well approximation can also be applied to the holes in the valence well to determine their allowed energy levels. So quantum effects have altered the band structure to create discrete allowed energy levels within the conduction and valence bands. Although this infinite potential well approximation can be used to determine rough estimates for the allowed energy levels, a more appropriate model accounts for a particle confined to a finite potential well.

In modifying the infinite well to a finite one, it is necessary solve the Schrödinger equation both inside and outside the well since there now exists a probability that the particle can be found outside the well. Considering a finite well of energy depth V_0 , extending spatially from $-d/2$ to $d/2$, and a particle of energy ϵ less than V_0 confined within, the Schrödinger equation for a particle inside the well ($-d/2 < x < d/2$) becomes

$$\frac{d^2\psi}{dx^2} = -k^2\psi \quad [2.4-7]$$

where

$$k^2 = \frac{2m^*\epsilon}{\hbar^2} \quad [2.4-8]$$

Outside the well ($x < -d/2$ and $x > d/2$) the equation is

$$\frac{d^2\psi}{dx^2} = \beta^2\psi \quad [2.4-9]$$

where

$$\beta^2 = \frac{2m^*(V_0 - \epsilon)}{\hbar^2} \quad [2.4-10]$$

The solution to [2.4-7] is sinusoidal while exponentials provide solutions to [2.4-9]. The constraint that ψ remains finite as $x \rightarrow \pm\infty$ limits the exponential solutions of [2.4-9] to decaying functions, while the continuity of ψ and its first derivatives at the $-d/2$ and $d/2$ interfaces provide a set of boundary conditions. Since the particles in the potential well may have different effective masses than the barrier regions surrounding it, the continuity of the first derivatives is weighted by these masses. Together, these constraints and boundary conditions create a set of transcendental equations relating k with β and whose solutions are the allowed energy levels (eigenvalues) within the well. These transcendental equations are

$$k \tan \frac{kd}{2} = \frac{m_w^*}{m_b^*} \beta \quad [2.4-11]$$

and

$$k \cot \frac{kd}{2} = -\frac{m_w^*}{m_b^*} \beta \quad [2.4-12]$$

where m_w^* is the effective mass within the well and is used in computing β , while m_b^* is the effective mass outside the well (in the barrier) and is used in determining k . Although there is no closed form solution of these for ϵ , numerical or graphical methods can be employed. Now that quantum effects have been used to determine the allowed energy levels, they must also be applied to the density of states function.

The presence of a quantum well reduces the development of the density of states function as discussed in Section 2.2 from three dimensions to two, since the quantum well is effectively a two-dimensional structure. Instead of determining the number of

states in the volume between spheres of energy E and $E + dE$, the number of states in the area between circles of energy E and $E + dE$ must be found. This area is

$$dA = 2\pi k dk = 2\pi \frac{\pi\sqrt{8m^*E}}{h} \frac{\pi\sqrt{2m^*dE}}{h\sqrt{E}} = \frac{8\pi^3 m^* dE}{h^2} \quad [2.4-13]$$

which is interestingly independent of the energy, E . A single state occupies an area of $4\pi^2/A$ in momentum space, where A is the real space crystal area. Finally incorporating two possible spins, the two-dimensional density of states becomes

$$g(E)dE = \frac{4\pi m^*}{h^2} dE \quad [2.4-14]$$

This density of states function describes the number of allowed energy states per unit area for each quantized energy. Thus, the total number of allowed energy states becomes a step function as shown for an infinitely deep quantum well in Fig. 2-8. The density of states function is enveloped by the three-dimensional density of states function applied to a volume with thickness equal to that of the quantum well width. For a finite quantum well, the steps in the density of states function occur at the energy eigenvalues from the transcendental function in [2.4-11] and [2.4-12], and are enveloped by the 3-D density of states function.

Although this approach yields the relative positions of the allowed energy states within the well region, the actual positions are determined by first locating the conduction band minimum and valence band maximum of the well bulk material with respect to those of the barrier material. The simplest method of measuring these levels and therefore finding the well depths is to use the electron affinity of the material. This energy is the separation between the conduction band edge and the vacuum level, and is the minimum energy necessary to completely free an electron from the semiconductor

potential (8: 288). If a conduction electron is imparted with exactly the electron affinity energy, it emerges from the semiconductor surface and appears in the surrounding vacuum with no excess energy. Any excess energy initially bestowed upon the electron results in the electron having a kinetic energy once liberated. Electron affinity is a material constant which can be used to relate the positions of the barrier conduction and valence bands to those of the well. With the conduction and valence well depths

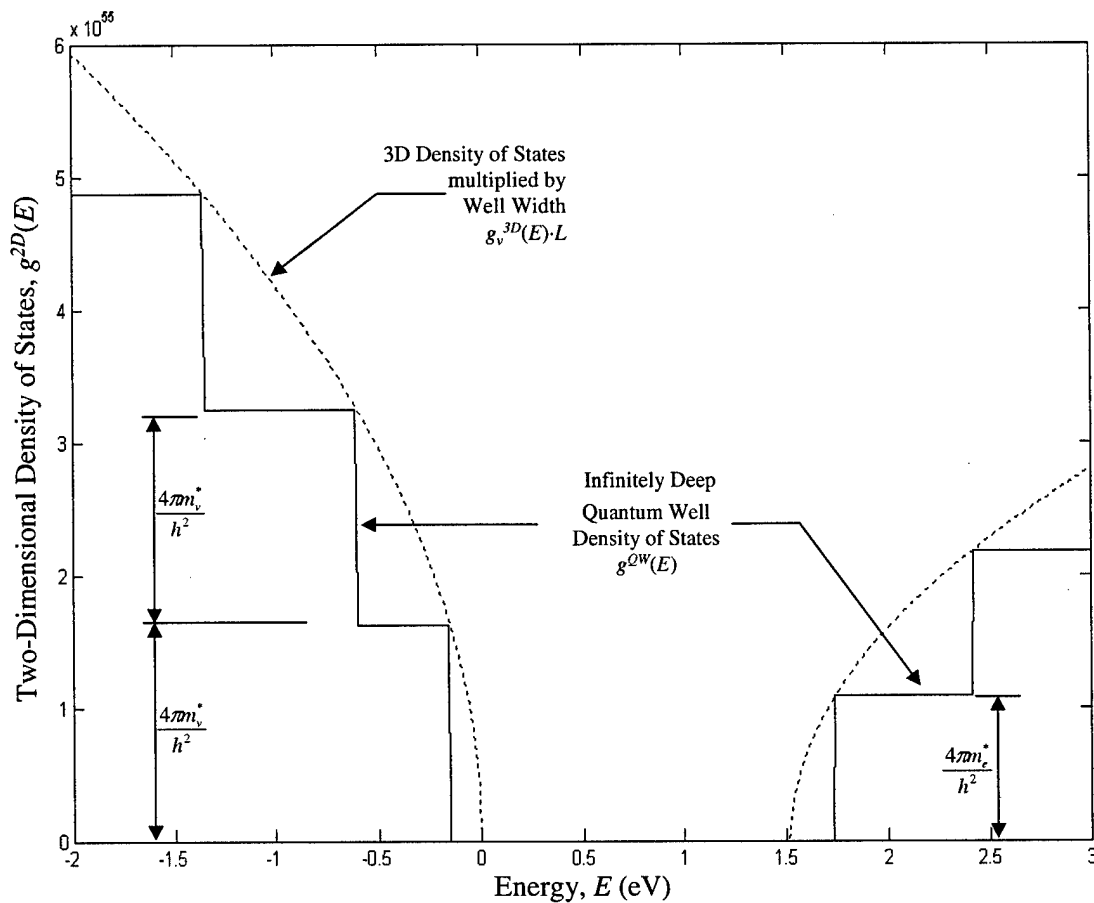


Fig. 2.8. Two-dimensional density of states function. An infinitely deep quantum well structure with discrete allowed energy levels in the conduction and valence bands has a step-like density of states function (solid) which is enveloped by the three-dimensional density of states function applied to a well-width thick semiconductor (dotted).

determined, the number of allowed states can be ascertained and their positions approximately determined using the infinite-well model. There is, however, one last parameter whose effects must be evaluated before the exact conduction and valence band levels can be fixed—strain.

2.5. Strain in Multi-layer Structures

As stated previously, a quantum well structure is a double heterojunction created by sandwiching an ultrathin semiconductor material between two unlike semiconductor barrier materials. For this double heterojunction to be a seamless connection creating a single crystalline structure, the atomic spacing of the materials on either side of the junction must be altered slightly. This produces tension or compression of the lattices so that, at the junction, the lattice spacing is matched. In a heterojunction, where the materials on either side of the junction are quite long, strain cannot be maintained above a “critical thickness” and is relieved via dislocations. In a quantum well structure where the center material is only a few hundred Angstrom thick (or less), the strain effects are significant since the entire region is either compressed or expanded. This forced lattice-matching condition, and the strain it induces within the well region, affects the energy structure by changing the energy gap and the relative positions of other nearby conduction or valence bands.

As shown in Fig. 2-1, the relative positions of the energy bands depend on the interatomic spacing of the compound. The hydrostatic component of the strain changes the positions of the bands by altering the atomic separation and thus changes the energy gap of the material. If the material is compressively strained, where the lattice is forced

into a closer separation than in equilibrium, the energy gap increases and emission wavelengths are blue-shifted. However, if the material is subject to tensile strain, the energy gap decreases and wavelengths are red-shifted.

Strain also has a shear component that affects the positions of the heavy and light hole bands. In an unstrained semiconductor, the heavy and light hole bands reach a maximum at the same point in the $E-k$ diagram. Due to differences in their effective masses, the light hole band slopes to lower energies than the heavy hole band as momentum increases. The introduction of strain breaks this degeneracy at $k = 0$, splitting the light from the heavy hole band, as shown in Fig. 2-9. Compressive strain acts to push the light hole band down, away from the heavy hole band maximum. Under tensile strain, the light hole band maximum is actually above that of the heavy hole band. In this

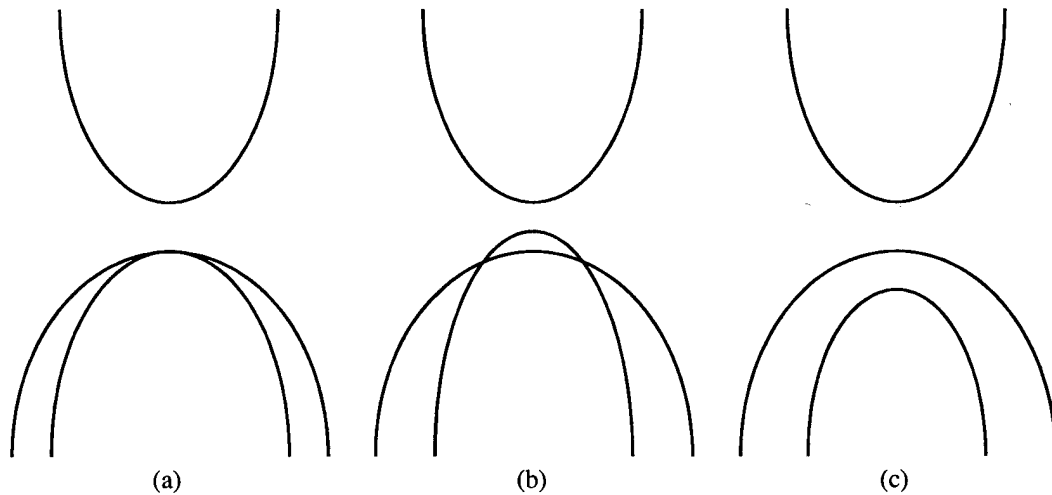


Fig. 2-9. Strain effects on valence band structure. The heavy and light hole bands of a semiconductor under no strain have a degeneracy at $k = 0$ in $E-k$ space (a). This degeneracy is broken under strain. Tensile strain (b) shifts the light hole band maximum higher than that of the heavy hole band, while under compressive strain (c), the light hole band is pushed down from the heavy hole band.

case, the maximum of this shifted light hole band becomes the new valence band energy level, thus significantly reducing the energy gap. For example, for $\text{In}_x\text{Ga}_{1-x}\text{As}$ grown on GaAs which is compressively strained, the heavy and light hole bands are split by $0.42x$ eV at room temperature for small indium mole fractions, x (12: 67).

Finally, strain also modifies the carrier effective masses. By compressing or expanding the lattice, the energy potential induced by the atoms of the lattice and experienced by free carriers changes. With effective masses calculated from the potential they are subject to, a change in this energy potential has significant consequences to all carrier effective masses.

3. Experimental Procedure

This chapter provides a detailed description of the equipment and samples used during the photoluminescence study of the quantum well structures. Figure 3-1 is a schematic diagram of the photoluminescence experiment developed for this study. Also included are explanations for the preparation and conduction of the experiment, as well as associated difficulties overcome during execution.

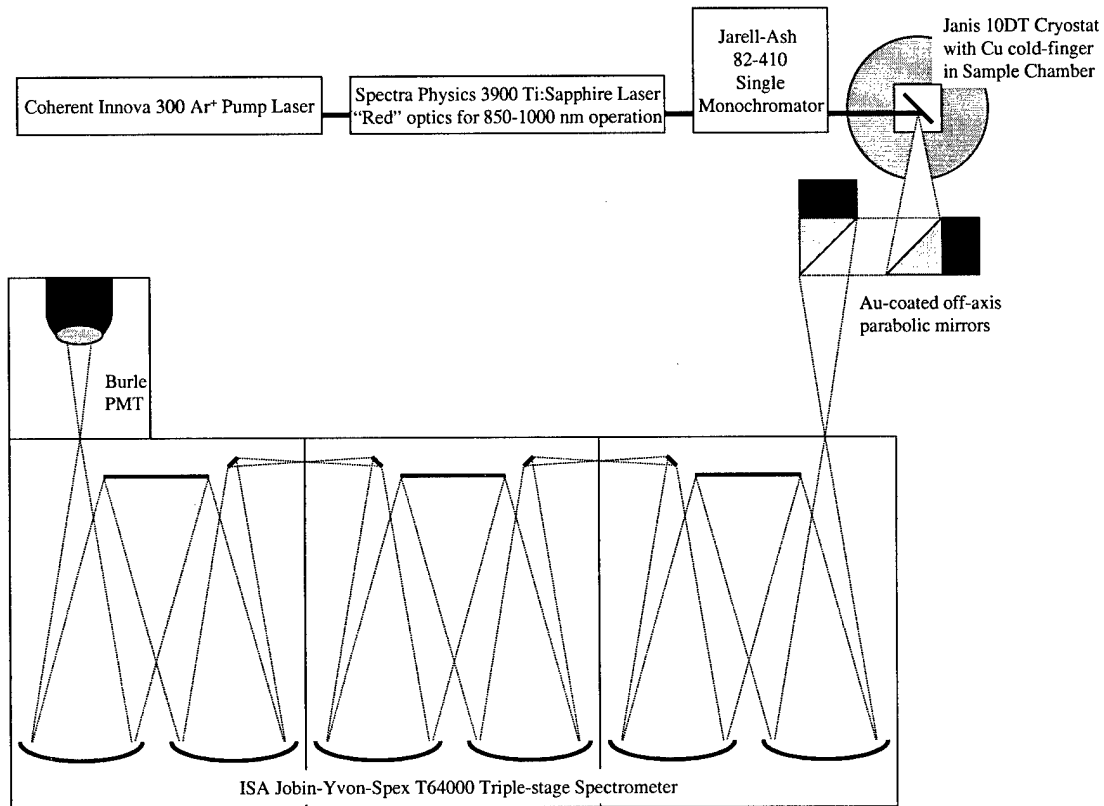


Figure 3-1: Diagram of experimental configuration for photoluminescence studies. Variable excitation energy Ti:Sapphire, pumped by an argon ion laser and filtered by a single monochromator, is used to excite the sample. The resultant photoluminescence is captured and directed into the spectrometer where it is spectrally separated and detected by the PMT.

3.1. Configuration

The cornerstone of the experimental configuration is the ISA Jobin-Yvon-Spex model T64000 triple-stage spectrometer. The two-stage, subtractive premonochromator provides initial filtering of the input signal and reduces stray light noise. A computer with the Dilor LabSpec 3 software, tied to the ISA motor controller, manages grating positions, intermediate slit widths and the high voltage supplied to the photomultiplier tube (PMT). Initially, a Burle C31034 gallium arsenide PMT was used which furnished superior responsivity to 850 nm. However, it was replaced with a Burle S1 silicon PMT to extend the detector response further into the infrared. Although the LabSpec 3 software could display the output current from the PMTs, a photon counting scheme was developed whereby the PMT output is amplified by a Stanford Research model SR445 4-channel amplifier, then fed to a Stanford Research SR400 gated photon counter whose trigger is controlled and output received by a separate computer running LabWindows. This method of data collection offers greater signal-to-noise ratios, as well as data visibility, which is discussed further in Section 3.4.

To provide maximal signal entering the spectrometer, reflective optics, rather than refractive, are employed. Gold-coated off-axis parabolic mirrors were matched to the effective f -numbers of the spectrometer and the sample chamber window geometry. In this configuration, the maximum cone of rays from the sample, limited by the chamber window, would be collected by the first mirror and collimated so the second mirror could both focus the beam to a waist at the spectrometer entrance slit, as well as fill the spectrometer grating.

Using CryCon grease for maximal thermal conductivity, samples were mounted on the copper cold finger of a Janis model 10DT cryostat which was capable of operation at 4.2 K temperatures through liquid helium cooling with no vacuum pumping. A Lakeshore Cryotronics model DRC-82C temperature controller monitored sample temperature and increased temperatures through a current supply to the cold-finger-mounted heater.

The sample was excited by the variable-wavelength output of a Spectra-Physics model 3900 Ti:Sapphire laser, concentrated onto a 1 mm^2 spot with a Newport 88.30 mm focus lens. Aligned with the “red” optics set, this laser provided excitation between approximately 850 nm and $1 \mu\text{m}$. A Coherent Innova 300 argon ion laser was used to pump the Ti:Sapphire. The output of the Ti:Sapphire was filtered by a Jarrell-Ash model 82-410 single monochromator to prevent possible argon plasma lines from propagating through the system into the triple monochromator.

3.2. Sample Information

The sample studied was a 50 Angstrom (\AA) indium gallium arsenide single quantum well surrounded by gallium arsenide barrier regions. The mole fraction of indium was 0.2 ($\text{In}_{0.2}\text{Ga}_{0.8}\text{As}$), meaning that 20 percent of the gallium atoms in the binary GaAs structure were replaced with indium atoms to form this ternary quantum well. Although this sample was intended to have $5 \times 10^{17} \text{ cm}^{-3}$ beryllium acceptors doped only in the well region, through either diffusion or error in fabrication, acceptors were also introduced in the barrier regions (as will be shown in section 4.3). The entire structure was deposited on a GaAs substrate using molecular-beam epitaxy (MBE). This process

impinged molecular beams of indium, gallium, arsenic, and beryllium to build layers on a properly prepared substrate under high vacuum. The actual compositions and dopings of the barrier and well regions are determined by manipulating the arrival rates of the atoms and the temperature of the substrate surface.

Given the material constants listed in Table 3-1, the number and position of allowed conduction and valence band levels were determined using the theory developed previously in Section 2.4. The resulting energy band diagram is shown in Fig. 3-2.

Table 3-1. Material constants for GaAs, InAs, and strained $\text{In}_{0.2}\text{Ga}_{0.8}\text{As}$. Unless otherwise noted, all values are for $T = 7$ K.

| Physical Property | GaAs ^a | InAs ^b | $\text{In}_{0.2}\text{Ga}_{0.8}\text{As}$ ^c |
|---------------------------------------|-------------------|-------------------|--|
| Direct Bandgap, E_g (eV) | 1.5189 | 0.4199 | 1.2213 |
| Electron Mass, m_c^* (m_0) | 0.067 | 0.0239 | 0.069 |
| Heavy Hole Mass, m_{hh}^* (m_0) | 0.51 | 0.43 | 0.16 |
| Light Hole Mass, m_{lh}^* (m_0) | 0.082 | 0.026 | 0.096 ^d |
| Heavy Hole-Light Hole Split (eV) | - | - | 0.084 ^e |
| Band Offset, $\Delta E_c:\Delta E_v$ | - | - | 0.6:0.4 ^f |
| Beryllium Binding Energy (meV) | 28.0 | | 18.0 ^g |

^a (6: 101-113)

^b (6: 133-141)

^c (1: 277)

^d (3: 923)

^e (12: 67)

^f (10: 536)

^g (5: 180-182)

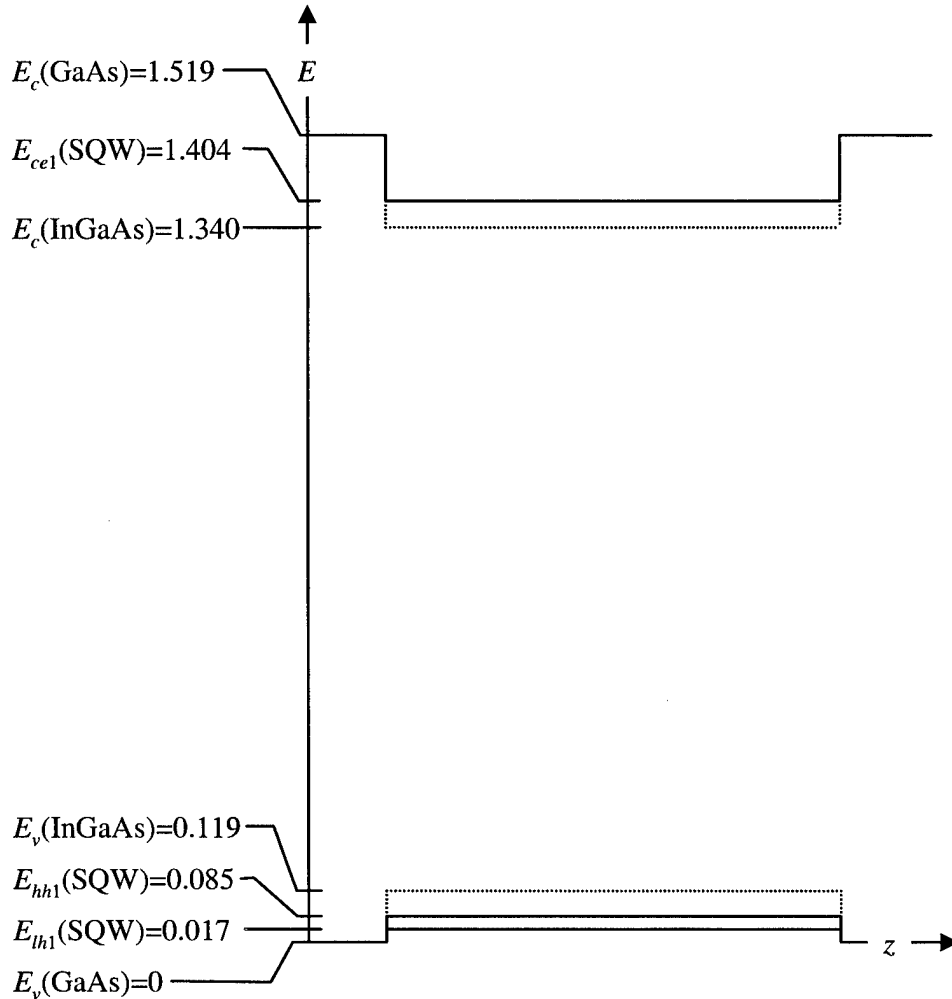


Fig. 3-2. Theoretical energy diagram of allowed quantum levels for a 50\AA $\text{In}_{0.2}\text{Ga}_{0.8}\text{As}$ single quantum well in GaAs. This diagram is based on the material constants expressed in Table 3-1 and the finite potential well theory developed in Chapter 2.

3.3. Execution of Experiment

This section details the process used in conducting the photoluminescence experiment. It begins with general procedure for laser operation, mirror alignment, sample cooling, and monochromator settings used in all three studies (excitation, temperature, and power). It concludes with specific methods employed which differ for each study.

After the Ti:Sapphire laser was aligned using a few hundred milliwatts of pump power from the argon ion laser, the pump power was increased to approximately five watts, yielding up to eight milliwatts of laser excitation power in the 865 nm to 1 μ m range. The output wavelength of the Ti:Sapphire laser was selected using a birefringent crystal turned by an actuator. Power measurements of the excitation beam were taken with a Fieldmaster model FM power meter with a Coherent model LM-2 detector head located at the sample chamber entrance window. To ensure this was the maximum excitation power, the output and high-reflectance mirrors of the Ti:Sapphire and the single (filtering) monochromator were adjusted for each wavelength. By increasing the argon ion laser pump power to nine watts, the Ti:Sapphire output increased to a maximum of 39 mW of power. This is the method used for controlling the excitation laser power during pump power studies of the sample.

With the Ti:Sapphire excitation laser now focused on the sample chamber, the off-axis parabolic mirrors must be aligned to maximize collection of the sample photoluminescence and reflection into the triple monochromator. The rough surface of the copper cold-finger acts a diffuse reflector and thus a point source of spherically diverging light. With the second off-axis parabolic mirror removed, the position of the first mirror could be maximized for the geometry of the sample chamber. By placing a two-inch diameter circle (equal to the diameter of the mirror) on a screen a few feet from the mirror, the orientation (rotation and two-axis tilt) and position (x , y , and z) could be established which took the diffuse-reflected laser light and collimated it into a two-inch beam. By moving the circle farther from the mirror and again adjusting the mirror orientation and position, beam collimation is verified. The second parabolic mirror could

then be replaced and positioned such that the entire two-inch beam is collected by the mirror surface. Rotation, tilt, and focal distance were rough adjusted to steer the beam into the monochromator entrance slit. Excitation laser power was reduced by decreasing argon pump power and the monochromator was moved to the wavelength of the excitation beam. Using a Keithley Instruments model 414A picoammeter to monitor the PMT output current, the orientation and position of each mirror were adjusted to maximize the signal current. Since the sample is not coplanar with the coldfinger surface due to the thickness of the CryCon grease, the orientation and position of each mirror as well as the excitation laser focusing lens were again adjusted to maximize the signal current from the sample photoluminescence.

Before conducting photoluminescence studies, the sample under observation must be cooled often to liquid helium (4.2 K) temperatures. However, before the sample can be cooled, the cryostat must be precooled so the liquid helium is not immediately vaporized. To help isolate the Janis model 10DT cryostat from the environment, a vacuum pump evacuates outer and inner jackets while another pump evacuates the sample chamber itself. After the sample chamber is purged with dry helium gas to remove any water or residual air, the inner reservoir is over-pressurized with dry helium gas and liquid nitrogen is added to the outer reservoir to begin precooling. After approximately six hours, the system should be sufficiently precooled and liquid helium could be introduced into the inner reservoir. During transfer an American Magnetics model 110A liquid helium level meter is employed to monitor the amount of coolant. A piston valve controls the flow of liquid helium from the inner reservoir into the sample chamber. Although this process must be completed for all studies, specific modifications

can be made for application to temperature studies. By monitoring the sample temperature on a Lakeshore Cryotronics model DRC-82C temperature controller and changing the liquid helium flow rate by adjusting the piston valve, the sample can be held constant at any temperature above that of liquid helium.

After completion of the above steps, photoluminescence studies were now ready to be conducted. However, to determine the wavelength steps made by the movement of the gratings, calculation of the spectral resolution of the system was necessary. The resolution of a spectrometer is based on the grating characteristics and the exit slit as

$$\Delta\lambda = \frac{aw}{mf} \quad [3.3-1]$$

where f is the spectrometer focal length, w is the width of the exit slit, a is the grating spacing, and m is the order for the blazed grating. Although the overall wavelength resolution could be complicated in a triple monochromator, here it is simplified by having similar gratings and focal lengths in each of the three stages. The system resolution is then dependent only on the exit slit width of the last stage and the intermediate slits only provide reduction in ambient and diffracted light, thus reducing noise levels. Most experiments were run with 1 Å wavelength steps of the grating motor, therefore the exit slit width was chosen to match this value closely. With the exit slit at 75 μm, the 0.64 m focal length spectrometer with 900 lines/mm gratings produced a 1.29 Å resolution in the first order. The entrance and first intermediate slits were opened to 300 μm while the second intermediate slit width was chosen to be 100 μm.

This completes the discussion of procedures needed to run a general photoluminescence study. Also covered above were the methods of altering these basic preparations in conduction of temperature and pump power studies. In running a

photoluminescence excitation (PLE) study, it is necessary to collect the photoluminescence data while monitoring, not only the sample temperature and excitation laser power, but also, the excitation wavelength. Therefore, it is necessary for the spectral scan to include the laser wavelength, however this reflection off the sample was too intense, saturating the detector. For this scan, two neutral density filters (each with 3.0 optical density) were placed at the entrance to the monochromator to step down the excitation laser power. Once the wavelength of the laser was observed and recorded, the filters could be removed and the scan restarted 5 Å beyond the laser wavelength. Sufficiently far from the high-power excitation beam, collection continues without concern for damaging the detector.

Although the three studies could now be conducted using the LabSpec 3 software for signal collection, there were difficulties encountered which need to be rectified before data collection could be optimized to begin observing low-intensity PL events such as hot-electron transitions. These obstacles are detailed in the next section as well as the methods employed in overcoming them.

3.4. Difficulties and Lessons Learned

The configuration and procedures outlined above provided for efficient data collection of pump power, temperature, and PLE studies of the samples, once minor obstacles were resolved. The poor signal sensitivity of the vendor-supplied collection software gave rise to the need to consider alternate methods of data collection. The solution was to establish a photon-counting scheme. However, this created new problems since separate computers were needed for data collection and spectrometer control.

Photon counting required choosing a discriminator level which would distinguish between detector noise and the actual absorption of a photon by the detector. This level was chosen to maximize the signal-to-noise ratio of the photoluminescence. This section describes these three data collection problems and the approaches used in overcoming them.

Although the Dilor LabSpec 3 software was able to display the current signal produced by the PMT, its signal sensitivity was limited. The intensity displayed by the software zeroed out before the PMT noise floor was reached. Without the ability to show the detector noise current, small signals just above the noise level also could not be observed. To improve the sensitivity of the reading of the PMT current, a photon counting approach was employed using the SR400 gated photon counter. This approach unfortunately required a separate computer to trigger the SR400 and collect its count output.

With two computers controlling the movements of the spectrometer mirrors separately from the triggering of the photon count, timing was paramount. If the computers were perfectly synchronized, the photon count would trigger exactly when the mirrors moved. However, this proved impossible in reality. Instead, an attempt was made to ensure that a maximum of one mirror movement occurred during each photon collection gate. With no movement during the collection period, the count represents the number of photons at one specific wavelength, while with one movement, averaging occurs between two wavelengths. By moving sufficiently slowly and in small wavelength intervals, mirror movements could be better monitored and the effects of averaging could be minimized due to the resolution set by the spectrometer slits.

Once an optimal timing scheme was determined, the PMT current discriminator level required adjustment to maximize the signal to noise ratio (SNR). This was accomplished by varying the voltage applied to the PMT and the discriminator level set on the SR400, and evaluating the ratio of the photon count at the gallium arsenide conduction band to acceptor level transition (signal) to the photon count corresponding to an energy level less than the energy gap. Fig. 3-3 shows the constant PMT voltage contours and a maximum SNR at 1400 V applied to the PMT and 70 mV for the discriminator.

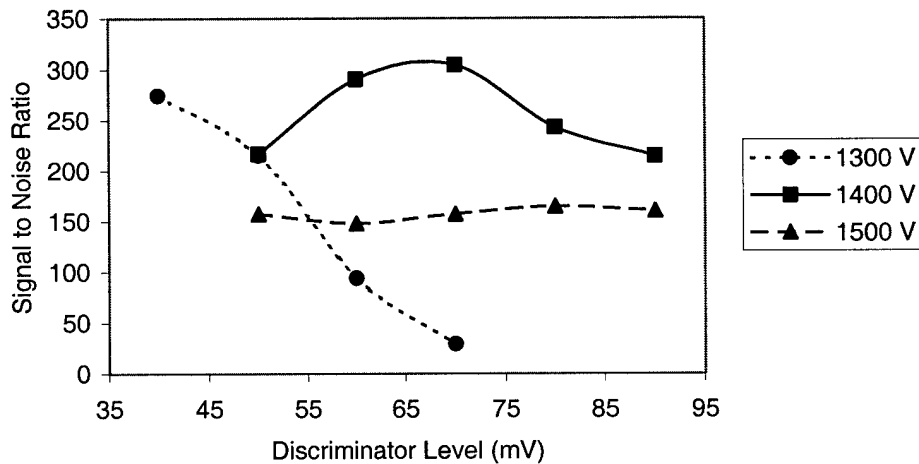


Fig. 3-3. Constant PMT voltage contours used to determine the optimal photon counting discriminator level. The signal count was measured at the conduction band to acceptor level of gallium arsenide while the noise at a wavelength corresponding to an energy much less than material band gap. The maximum SNR occurs for a 1400 V PMT voltage and 70 mV discriminator level.

4. Results and Discussion

In the previous sections, a review of semiconductor theory formed the basis for the analysis of the InGaAs single quantum well structure and an experimental setup was proposed that would allow for the confirmation of this theory. Here, the photoluminescence studies, performed at varying excitation energies and various temperatures, are examined either to validate the material constants presented in Table 3-1 or to propose adjustments to their values.

4.1. Photoluminescence Excitation

Photoluminescence excitations were performed by varying the Ti:Sapphire laser wavelength. Beginning with energies below that of the InGaAs energy gap, the laser wavelength was steadily decreased to that sufficient to excite the InGaAs quantum well without exciting the GaAs barrier. By selectively exciting the well region, transitions can be separately viewed, providing for more efficient band analysis. With the sample temperature fixed at 7 K, an excitation wavelength of 916.5 nm (1.3528 eV) is insufficient to excite electrons from the first (highest) quantized heavy hole state into the first (lowest) allowed conduction level as shown in Fig. 4-1. This figure also shows the development of this first transition as the excitation energy increases. At an excitation wavelength of 912.4 nm (1.3589 eV) the spontaneous emission from the first conduction state to the first heavy hole state begins to form and a shoulder in the low energy side is apparent.

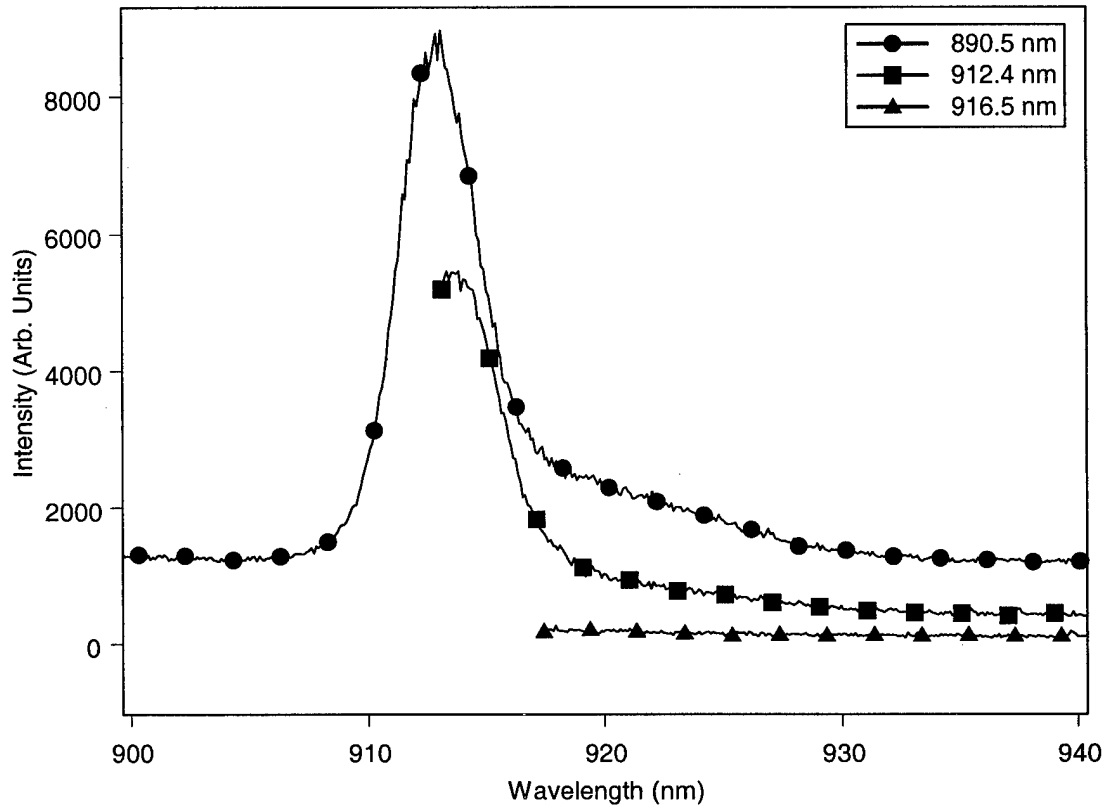


Fig. 4-1. Photoluminescence excitation study of the InGaAs/GaAs quantum well structure at 7 K. For wavelengths below 916.5 nm, no photoluminescence is observed. As the excitation energy increases, a peak at 911.7 nm emerges as does a shoulder at 917.5 nm.

At higher excitation energies, such as the 890.5 nm (1.3923 eV), the quantized conduction to heavy hole transition is fully formed, peaking at 911.7 nm, and the conduction to acceptor shoulder remains at 917.5 nm. The beryllium transition is initially identified since it only appears when the excitation energy is sufficient to excite electrons from the heavy hole band to the conduction band. These electrons are then able to relax to either the empty acceptor level or back to the heavy hole band. Since the acceptor level is empty at low temperatures with no electrons available to contribute to the conduction band, the first source of these electrons is the first heavy hole band.

Therefore, only with excitation energy high enough to pump electrons from the heavy hole into the conduction band will there be photon emission observed.

With an almost completely empty acceptor level at the temperature (7 K) maintained during this experiment, it would seem that the $5 \times 10^{17} \text{ cm}^{-3}$ beryllium ions would accept most of the radiating electrons and therefore be the prominent peak. This is not observed since the laser intensity is 30 mW focused onto a 1 mm^2 spot. At this wavelength, this equates to pumping the sample with 1.34×10^{17} photons onto an area containing only 1×10^{14} acceptor ions (for a 0.5 mm thick semiconductor). If only one photon in one hundred were absorbed, there would still be more conduction electrons than empty acceptors by an order of magnitude. Thus, for a high laser pump power, the heavy hole transition dominates that of the acceptor and the data shown in Fig. 4-1 is accounted for.

Further proof that this low energy shoulder is the acceptor transition will be provided through the temperature study since the acceptor level should thermally populate at a few hundred Kelvin. Therefore, it will be necessary to explore whether the acceptor transition weakens and disappears as temperature increases.

Returning to the photoluminescence excitation study, it is concerning that, even at higher excitation energies, the conduction to quantized light hole band is not observed. If a light hole band is allowed within the well, its electrons should be pumped into the conduction band by the 890.5 nm excitation line. However, there is no evidence of a conduction to light hole radiative recombination. One possible explanation is that the strain induced by lattice matching the InGaAs well to the GaAs barriers was sufficient to displace the light hole band far enough away from the heavy hole band that there are no

allowed light hole bands within the well. Another possibility is that at these low temperatures, the Fermi-Dirac distribution does not penetrate far enough in the valence band to open holes in the light hole band. Any hole created by the excitation of an electron quickly thermalizes up to the heavy hole band. It is again necessary to perform temperature studies to confirm which hypothesis is correct.

4.2. Temperature Study

After observing only two transitions at low temperatures (7 K), it became necessary to observe the changes in the photoluminescence spectrum as temperature increased. The experiments addressed in this section were necessary to evaluate the following hypotheses suggested from the PLE: (1) the low energy shoulder is due to a conduction to acceptor transition, and (2) strain has split the light hole from the heavy hole band sufficiently to allow no quantized light hole band in the well.

With the laser wavelength fixed at 865.9 nm, the sample temperature was changed by adjusting the flow of liquid helium into the sample chamber. For reference, the 865.9 nm PLE spectrum used in the previous section is also used here as the 7 K spectrum. The results for sample temperatures of 7, 20, 40, 60, 80, 100, and 150 K are shown in Fig. 4-2. The first noticeable trait is that, as temperature increases, the peak wavelength is red-shifted. This conforms to semiconductor theory since as temperature increases, the energy gap decreases, thus the wavelengths should shift higher. This is also supported by the temperature dependence of the peak spontaneous recombination frequency, ν_p , from [2.2-13].

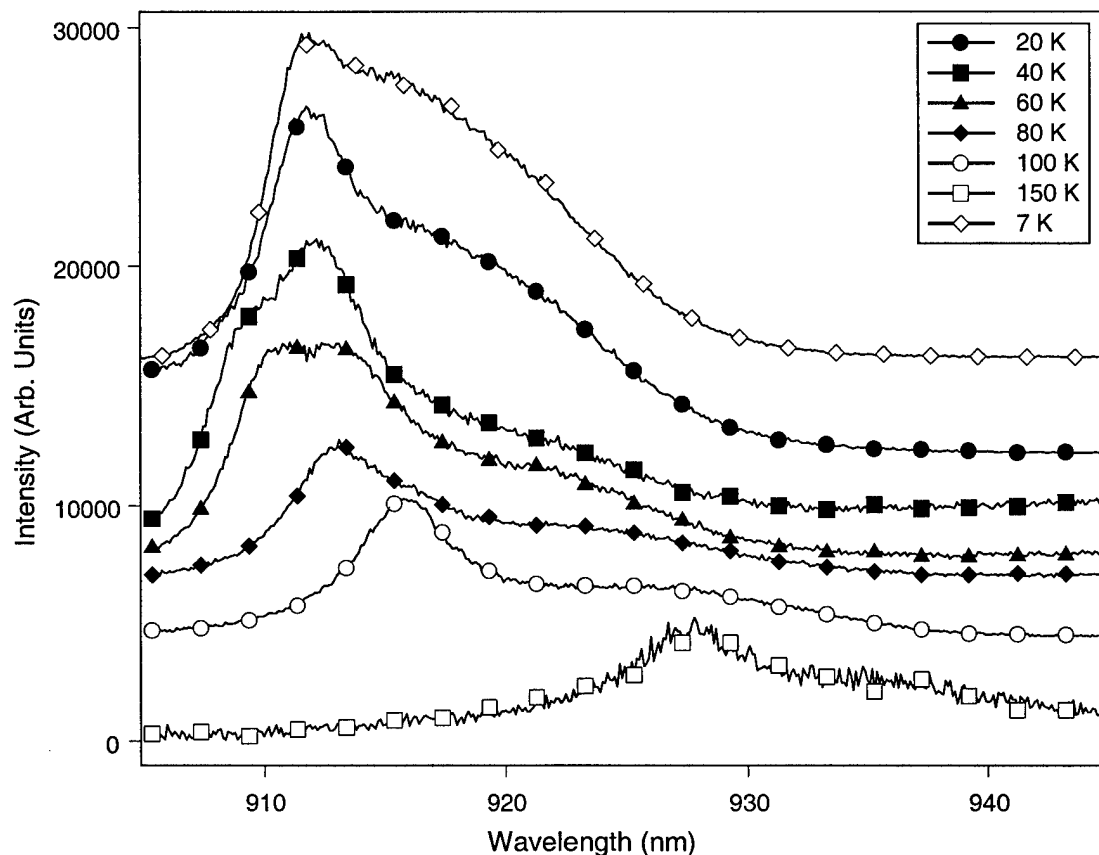


Fig. 4-2. Photoluminescence temperature study of InGaAs/GaAs single quantum well. As temperature increases, the prominent peak shifts to longer wavelengths which is consistent with energy gap shrinkage at high temperatures. A high energy shoulder also becomes prevalent as temperatures increase suggesting that a light hole band is allowed in the well region and becomes thermally depopulated. All were conducted with 40 mW at 865.9 nm laser excitation.

At low temperatures, the photoluminescence spectrum is dominated by the conduction to heavy hole transition due to the pump intensity. The shoulder on the low energy side is attributed to a conduction to acceptor transition. However at 40 K, a shoulder on the high energy of the dominant peak begins to emerge and by 60 K has become an equal peak with that of the conduction to heavy hole transition. This shoulder turned peak is determined to be a conduction to light hole transition.

This determination is made by eliminating other possible sources for this emission. It is not possible for this transition to be that of an electron relaxing from the first quantized conduction band to the second allowed heavy hole band. Transitions between the conduction and valence bands must conserve energy and momentum and, in a quantum mechanical structure, they must also conserve quantum number (11: 633). Thus, an electron in the first quantized conduction band can transition to any first quantized valence bands, but not to any other quantum states. Since this structure, in theory, only has one allowed conduction band, the only transitions (both for absorption and emission) are between the first heavy and light hole valence bands and the first conduction band. This is another important consequence; the only absorption events excite an electron from either the first quantized heavy hole or light hole bands into the only allowed conduction band. Therefore, even if higher quantum states existed in the valence well, there are no allowed transitions in to or out of them. The appearance of a second peak proves the presence of an allowed light hole band in the well, also proving the second initial hypothesis incorrect. But the first hypothesis on the assignment of the conduction to acceptor transition to the low-energy shoulder has not been addressed.

Since the acceptor energy is only a few meV above the valence band, it can normally be thermally filled with electrons at a relatively low temperature. However, even at 150 K, the low-energy shoulder is still apparent in the spectra. Given the doping concentration, temperature, and effective masses from Table 3-1, the extrinsic Fermi level can be determined from [2.3-3] as

$$E_F = \frac{E_g}{2} + \frac{3}{4}kT \ln \frac{m_v^*}{m_c^*} + kT \sinh^{-1} \left(\frac{N_d - N_a}{2n_i} \right) = 1.6 \text{ meV}$$

where n_i , the intrinsic carrier concentration, is determined from (7: 389)

$$n_i = 2 \left(\frac{2\pi\sqrt{m_c^* m_v^*} kT}{h^2} \right)^{3/2} e^{-E_g/2kT} \quad [4.2-1]$$

With the acceptor energy 9.86 meV above the first heavy hole band from the 150 K temperature study, the Fermi level is only 8.26 meV below the acceptor level in the well. At this temperature, the Fermi-Dirac distribution predicts this state is only 65.5% thermally filled with electrons. There are therefore still over $3 \times 10^{17} \text{ cm}^{-3}$ acceptor sites capable of receiving the electrons transitioning from the conduction band. Then the initial hypothesis that the low-energy shoulder is the conduction to acceptor transition is not disproven. The decreasing strength of the beryllium transition with respect to the light and heavy hole transitions as temperature increases also follows the theory.

By fitting gaussian functions to the temperature study spectra, the exact peak transition wavelengths can be determined. Fig. 4-3 shows these transition energies as a function of wavelength for the first quantized conduction band (ce1) to the first heavy hole (hh1), first light hole (lh1), and acceptor (Be) levels. In bulk semiconductors, the temperature-induced change in the bandgap energy, E_g , is given by the Varshni equation (14: 149)

$$E_g(T) = E_g(0) - \frac{\alpha T^2}{\beta + T} \quad [4.2-2]$$

Using this functional form and fitting the data of Fig. 4-3, the light hole data set can be regressed back to 7 K so its position with respect to the heavy hole band can be determined at low temperatures. Furthermore, both the heavy hole and beryllium transition lines can be estimated for 300 K, and the acceptor binding energy compared

with the value from Table 3-1. The α and β coefficients for each of the transitions is given in Table 4-1.

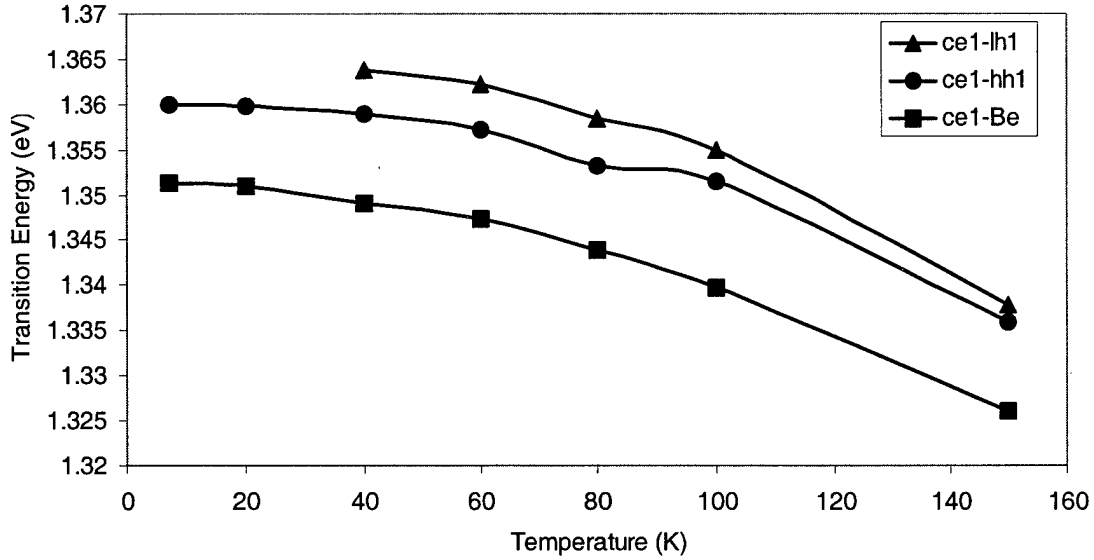


Fig. 4-3. Temperature dependence of transition energy. As temperature increases, the material bandgap is reduced and transition energies decrease. The general shape of these data sets can be fit to the Varshni equation given in [4-2.2]. From this fit, the data set can be regressed to absolute zero or interpolated to room temperature.

Table 4-1. Varshni α and β coefficients fit to the data in Fig. 4-3. Also given are the functional approximations for the transition energies extrapolated to $T = 0$ K and 300 K.

| Transition | α (eV/K) | β (K) | $E(0\text{ K})$ (eV) | $E(300\text{ K})$ (eV) |
|------------|-------------------------|----------------|-------------------------|---------------------------|
| ce1-lh1 | 3.1069×10^{-4} | 169.11 | 1.3664 | 1.3068 |
| ce1-hh1 | 9.691×10^{-2} | 107386 | 1.3605 | 1.2795 |
| ce1-Be | 2.186×10^{-3} | 1794.4 | 1.3513 | 1.2574 |

Extrapolating the data in Fig. 4-3 to 300 K, the difference between the heavy hole transition (1.2795 eV) and the beryllium transition (1.2574 eV) yields the acceptor

binding energy, 22.1 meV. This value is in good agreement with the value given by Loehr, *et. al* (5: 180-182), as 18 meV.

4.3. Material Parameters Evaluated

Using the data collected through the temperature and photoluminescence excitation studies and using the material constants from Table 3-1 as a starting point, structure parameters for energy gap, acceptor binding energy, heavy hole-light hole band split under strain, and band offset were evaluated. Two assumptions were made to ensure the parameters remained realistic. First, the beryllium binding energy is measured with respect to the first allowed valence band, here the first quantized heavy hole band, and not the valence band of a bulk InGaAs semiconductor; and second, the carrier effective masses make only minor changes to the level of allowed energies; therefore, they remain fixed to the values from Table 3-1.

Using the parameters for strained energy gap, band offset, and effective masses given in Table 3-1 in the finite potential well model described in Section 2.4, theory predicts a conduction to heavy hole transition at 940.0 nm. This transition can be seen in Fig. 3-2. The photoluminescence data collected for this research demonstrates this transition at 911.7 nm, considerably different than theory predicts. This difference between predicted and observed data can be explained by altering the parameters without changing the finite potential well model. Although four parameters were available to modify (strained energy gap, band offset, electron effective mass, hole effective mass), only revisions to the strained energy gap were intensely investigated since it offered the greatest variation to transition wavelength. Increasing carrier effective masses only

marginally increased the transition energy. Only a drastic increase, beyond realistic effective mass values, could yield this 28 nm change in transition wavelength. Similarly, the band offset only shifted the transition wavelength by a few nanometers for practical values of band offset (between 0.5 and 0.8 ΔE_c : ΔE_v).

Holding carrier masses constant, both in the InGaAs well and GaAs barrier regions, and the band offset fixed at 0.6, the strained energy gap was slowly increased from the original value of 1.2213 eV. At a value of 1.2715 eV, the solutions to the transcendental equations used in the finite potential well model yielded quantized energy states such that a transition from the first conduction band to the first heavy hole band was exactly at 911.7 nm. Thus a 4% increase in the strained energy gap resulted in an excellent match between theory and experiment.

The beryllium binding energy was determined to be 22.1 meV by extrapolating the Varshni fit of the data in Fig. 4-3 to 300 K. This value agrees to within 23% of the accepted value, 18 meV, given in Table 3-1. However, the accepted value was measured in a large epilayer of strained $\text{In}_{0.2}\text{Ga}_{0.8}\text{As}$ on GaAs, not a quantum well. More likely, the error can be attributed to extrapolating a few low temperature (up to 150 K) data points to 300 K.

Again using the Varshni fit parameters to extrapolate the heavy hole and light hole transitions to 300 K, the conduction to heavy hole transition is only 27.3 meV less than the light hole transition. From the finite potential well model with the effective masses of the electrons, heavy holes, and light holes fixed at the values given in Table 3-1 (0.069, 0.16, and 0.096 m_0 respectively), this separation is accounted for by a strain-induced split of 23.2 meV between the heavy hole and light hole bands. This value is

radically less than the 84 meV split determined by Singh (12: 67). This variation can be explained by looking at the differences in collection conditions. The 84 meV split was again measured in a large epilayer of strained $\text{In}_{0.2}\text{Ga}_{0.8}\text{As}$ on GaAs while the data presented here comes from a quantum well structure. This should only present a minor correction to predicted values, therefore the source of this drastic deviation is more likely the extrapolation model. While Singh's measurement was conducted at room temperature, needing no extrapolation, this "updated" value was based on extrapolation from a limited number of low temperature studies. In this case, the Varshni fit may be inappropriate.

Table 4-2. Summary of material constants evaluated in this thesis. Using the PLE and temperature studies, the strained energy gap, heavy hole-light hole energy split, and the beryllium binding energy were revised.

| Physical Property | Accepted Value | Observed Value |
|--|----------------------------|------------------------------|
| Strained Energy Gap at 7 K, E_g (eV) | 1.2213 ^a | 1.2715 |
| Heavy Hole-Light Hole Split (meV) | 84.0 ^b at 300 K | 23.2 at 300 K (extrapolated) |
| Beryllium Binding Energy (meV) | | 8.6 at 7 K |
| | 18.0 ^c at 300 K | 22.1 at 300 K (extrapolated) |

^a (1: 277)

^b (12: 67)

^c (5: 180-182)

5. Conclusions and Recommendations

Although this thesis revealed adjustments to only three parameters for one InGaAs/GaAs quantum well structure, the tenets applied herein could easily be expanded to evaluate other such structures regardless of composition or structure. Furthermore, this thesis created the initial groundwork necessary for other, more complex experiments. Such experiments as hot-electron photoluminescence studies will complete the modeling of these structures by evaluating the parameters held fixed here. The experimental architecture now exists within the Air Force Institute of Technology to perform a variety of photoluminescence studies at one location.

This thesis evaluated the theory regarding semiconductor quantum well structures and applied this theory to determine material characteristics for a 50 Å $\text{In}_{0.2}\text{Ga}_{0.8}\text{As}$ quantum well in bulk GaAs. Using a finite potential well model for both the conduction and valence bands in the quantum well region, the photoluminescence data adjusted the values for energy gap under strain, heavy hole-light hole energy split due to compressive strain, and the beryllium binding energy. From observation of the conduction to heavy hole and conduction to beryllium transitions at various temperatures, the beryllium binding energy could be extrapolated to room temperature using a Varshni functional form. This resulted in an increase from the accepted value of 18.0 meV to 22.1 meV. This disparity could be attributed to samples observed—a thick epilayer strained to match GaAs versus a quantum well strained heterostructure. The value used for the strained energy gap for low temperature measurements was also increased from 1.2213 eV to 1.2715 eV, changing the conduction and valence well depths, and therefore, the quantized energy states within. From this parameter adjustment, the model prediction for the

conduction to heavy hole transition matched that observed. Using the low-temperature data for the conduction to heavy and light hole transitions to extrapolate to room temperature, the strain-induced splitting of the heavy and light hole bands was reduced to 23.2 meV from 84 meV. This considerable difference is more than likely not caused by sample differences (epilayer versus quantum well), but to an inapplicability of the Varshni model. All of these parameter assessments were made while holding the carrier effective masses constant. Only through hot-electron photoluminescence could the carrier effective masses be evaluated through the observation of beyond-zone center transitions.

The theory and methods explored in deriving realistic parameters from empirical data is of prime importance to scientists and engineers worldwide who wish to predict quantum well structure performance without actual fabrication. Developing accurate models, applicable to a wide range of semiconductor structures, is the future of semiconductor analysis. The time and cost savings of this approach, as compared to experimental evaluation of a fabricated piece, is paramount.

Future research can be applied to fill the voids of this thesis by evaluating the material constants of other InGaAs/GaAs quantum well structures to verify that one model can effectively characterize all these devices. Furthermore, it is of great importance to begin characterizing these devices beyond zone center. Through the observation and collection of hot-electron photoluminescence, the material band structure can be fully characterized. This allows for the evaluation of the structure for application as an emitter, where direct gap transitions are desired, versus as a detector, where indirect gap transitions are acceptable.

APPENDIX A: HOT-ELECTRON PHOTOLUMINESCENCE

The original scope of this thesis was to evaluate semiconductor model parameters through hot-electron photoluminescence studies. These studies determine the band structure away from the $E-k$ zone center and can therefore evaluate the effective masses of carriers in the conduction and valence bands. Without these studies, photoluminescence excitation and temperature studies can be conducted to revise certain parameters, however the effective mass values would remain fixed and their contribution could not be addressed. This appendix describes relevant experiments previously performed by others which contribute to the setup and execution of this experiment, a significant milestone reached toward observing hot-electron PL and recommendations for completing this study.

A.1. Background

Early observation of hot electron photoluminescence, from 1969 into the early 1970s, is reviewed by Zakharchenya, *et. al*, (17: 143-144). Although faint hot electron PL was collected by Rebane and Sarri (9: 887) in 1969, it was not until over a decade later with the work of Zakharchenya, Hughes (2: 2953), and Kash (13: 949) that it was applied to identify carrier parameters. Significant experiments and limitations exposed are outlined in this section.

The observation of hot electron photoluminescence is highly dependent upon the concentration of free acceptors. In p-type crystals where $N_a > 10^{18} \text{ cm}^{-3}$, collisions of excited electrons with holes dominates radiative recombinations of hot electrons.

However, in moderately doped samples ($N_a \sim 10^{17} \text{ cm}^{-3}$) at sufficiently low temperatures to freeze holes to acceptors, structure in hot electron PL is clearly defined (17: 153). At much lower acceptor concentrations ($N_a < 10^{14} \text{ cm}^{-3}$), there are insufficient recombination sites into which the hot electrons may radiatively transition.

With $2 \times 10^{15} \text{ cm}^{-3}$ p-doped GaAs:Ge and an accurate knowledge of the conduction band structure, the valence band structure was determined by Fasol and Hughes with a precision of up to 1 meV. While most experimental techniques observe zone-center transitions, determining band properties around $k = 0$, then relying upon $k \cdot p$ calculations for band structure analysis, hot electron PL directly measures band structure away from $k = 0$. In their experiments, Fasol and Hughes used a tunable dye laser with excitation energies between 1.63 and 2.41 eV (corresponding to laser wavelengths between 514.5 and 760.6 nm). Their spectra showed oscillations in luminescence with the first peak corresponding to an immediate recombination of a photo-excited electron (from the heavy hole valence band) with an acceptor hole. Subsequent peaks of this oscillation are separated by the energy of one longitudinal-optical (LO) phonon. The spectra also shows recombinations of electrons initially excited from the light-hole valence band (2: 2955).

Although one of the most important applications of hot-electron PL is the determination of band structure beyond zone center and thus the effective masses of the carriers within these bands, hot electron PL can also be employed to evaluate electron scattering between conduction valleys. In 1988, Ubrich, Kash, and Tsang performed hot electron PL on $1.2 \times 10^{17} \text{ cm}^{-3}$ p-doped GaAs:Mg to measure intervalley scattering rates. With variable excitation energies from 1.57 to 2.54 eV (corresponding to wavelengths of 488.1 to 789.7 nm), the excitation power was controlled to maintain an injected carrier

density less than $3 \times 10^{15} \text{ cm}^{-3}$. This constraint was enacted since carrier densities above 10^{17} cm^{-3} would modify relaxation kinetics due to electron-electron collisions in the conduction band. Although they reported an unpolarized luminescence, they nonetheless polarized the laser along [100] and detected the hot electron PL at 90° to the laser (Ubrich: 949). This could offer a method of removing stray laser power from the hot electron signal desired. By linearly polarizing the excitation beam and using another linear filter at 90° to it, specularly reflected laser light is almost completely eliminated from entering the collection system.

Up until this point, the discussion of hot electron PL has been concerned solely with bulk samples. However, the band structure and scattering rates of semiconductor heterostructures could also be analyzed in a similar way. In 1991, Zachau, Kash, and Masselink expanded their previous hot electron work to report on the heavy and light hole band structures in quantum wells. This limits the measurement of the quantum well band structure since only laser energies insufficient to excite the surrounding barrier regions can be employed. In their experiment, laser excitation varied from 1.65 to 1.85 eV (670.2 to 751.4 nm) for GaAs/Aluminum gallium arsenide (AlGaAs) quantum well structures p-doped with $3 \times 10^{17} \text{ cm}^{-3}$ Be acceptors. The injected carrier densities were on the order of $5 \times 10^9 \text{ cm}^{-2}$ for the 50-100 Å wide wells. The result of this experiment was a much more complete model of the quantum well structure, including not only energy gap measurements but carrier effective mass values (16: 4048).

Hot hole PL is similar to hot electron PL except that the radiative recombination terminates in the split-off subband. PL spectra of lightly-doped n-type GaAs exhibits an intense peak around the energy gap (1.51 eV) with a significantly weaker structure at

1.85 eV. This weaker structure is attributed to hot hole PL and through PLE the split-off band can be diagrammed with respect to momentum, in a similar manner to mapping the conduction band using hot electron PL (17: 162).

A.2. Expected Data

The band structure of bulk GaAs near zone center can be approximated by parabolic E-k conduction and valence bands. The functional form of these bands was given as

$$E = \frac{\hbar^2 k^2}{2m_c^*} \quad [2.1-4]$$

using the electron effective mass in the conduction band and the heavy (or light) hole mass in the valence band. It was also previously shown that light of sufficient energy ($h\nu > E_g$) can be absorbed by the transition of an valence electron into the conduction band, conserving both energy and momentum. Although small, there exists a probability that the excited electron will immediately recombine with an empty hole in the acceptor level, thus emitting a photon. Since the acceptor level is a flat (with respect to k) energy level and the valence band bows down parabolically, the energy of the emitted photon will be less. This is shown in Fig. A-1. If the excited electron does not immediately recombine, it will begin to thermalize down to the conduction band minimum by creating LO phonons. After each emission of an LO phonon, the electron may again recombine with an empty acceptor, emitting another photon. Thus the signal expected for hot-electron transitions will be an initial peak due to immediate recombination and a set of replicas repeated at every LO phonon.

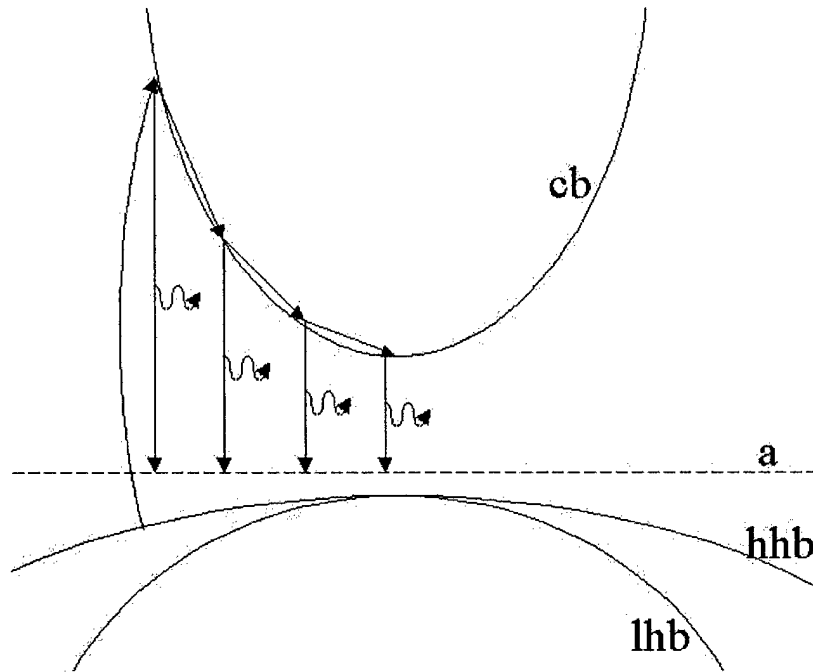


Fig. A-1. Energy diagram of hot electron recombinations. Electrons photo-excited (from the heavy hole (hhb) or light hole (lhb) valence bands) into the conduction band (cb) can immediately recombine with an acceptor level hole (a) producing a photon. As the electron thermalizes to the conduction band minimum through the creation of LO phonons, the hot-electron can still recombine with a hole in the acceptor level. This creates an oscillation in the photoluminescence, the period of which is the energy of the LO phonon.

The first hot-electron peak is important since, from observing it and knowing the laser excitation energy, the effective mass of either the electrons in the conduction band or heavy holes in the valence band can be determined. Using the parabolic approximation for both energy bands and a constant, E_A , acceptor binding energy and energy gap, E_g , the electron effective mass can be calculated as

$$m_e^* = m_{hh}^* \frac{E_L - E_{hep} - E_A}{E_{hep} + E_A - E_g} \quad [A.2-1]$$

by knowing the heavy hole effective mass, m_{hh}^* . In this equation, E_L is the laser excitation energy and E_{hep} is the transition energy associated with the hot-electron peak.

In conducting the experiment, it is often important to calculate the approximate location of the hot-electron transition given the excitation energy, using accepted values for the carrier effective masses. This approximate hot-electron energy is given by

$$E_{hep} = \frac{m_{hh}^*}{m_e^* + m_{hh}^*} E_L + \frac{m_e^*}{m_e^* + m_{hh}^*} E_g - E_A \quad [\text{A.2-2}]$$

and can be used in setting up the scan range for data collection.

A.3. Observation of the Longitudinal-Optical Phonon

Hot electron photoluminescence, where subsequent hot electron transition peaks are separated in energy by that of an LO phonon, is not the only place where the LO phonon can be observed. Even at a wavelength insufficient to excite a valence electron into the conduction band, the laser energy may produce another effect—the creation of an LO phonon and a vibration in the lattice. Since energy must be conserved, the laser excitation energy is reduced by the amount of energy of this newly created LO phonon.

The experimental setup and procedure used for conducting photoluminescence excitation studies of the InGaAs/GaAs single quantum well samples (described in Sections 3.1 and 3.3) was used in observing LO phonon replicas of the excitation laser line. Although phonon replicas were not observed in the bulk GaAs samples, they were recorded during PLE studies on the InGaAs/GaAs quantum well structures. The photoluminescence data, shown in Fig. A-2, shows two replicas for each laser excitation energy. Since the quantum well is a heterostructure composed of two different materials, the LO phonon energy is different in each material and the replicas are returned at two different wavelengths.

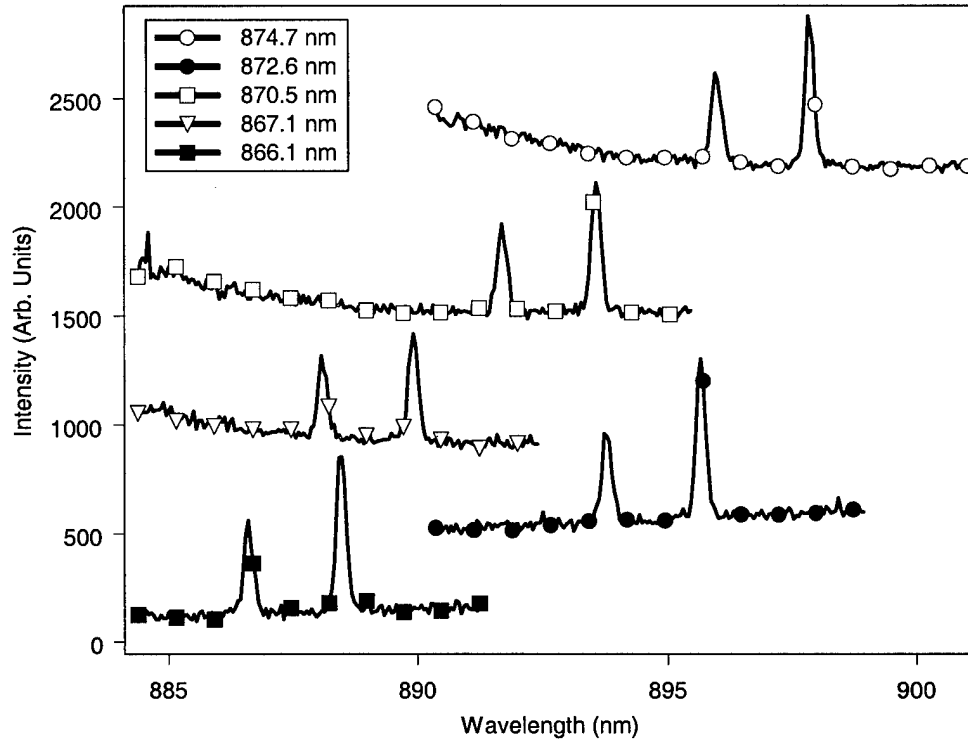


Fig. A-2. Observed longitudinal-optical phonon replicas of the laser excitation line. As the excitation wavelength shifts, the location of the LO phonon replicas shifts by the same energy. The first replica peak is associated with the InGaAs well material, while the second is from the GaAs barrier material. Conducted at 7 K.

From the five PLE data sets in Fig. A-2, the second (rightmost) replica is removed from the laser excitation energy by 33.49 ± 0.32 meV. This energy, identified as that of the GaAs barrier LO phonon, nearly agrees with the accepted value, 35.24 meV (6: 105). The difference in values is due to experiment temperature. The accepted value was measured at 300 K while the PL-derived value was at 7 K. The first (leftmost) peak is attributed to the $\text{In}_{0.2}\text{Ga}_{0.8}\text{As}$ quantum well material and is separated from the excitation energy by 36.40 ± 0.37 meV. The $\text{In}_{0.2}\text{Ga}_{0.8}\text{As}$ LO phonon energy is calculated as 34.18 meV from a linear interpolation of the GaAs LO phonon energy and that of InAs, 29.58 meV (6: 137). The source of error between observed and calculated is attributed to the

linear interpolation method used for calculation as well as experimental temperatures as before.

A.4. Recommendations

Although the observation of the longitudinal-optical phonon was a promising milestone leading to the observation of hot-electron photoluminescence, none was observed with either the bulk GaAs samples or the InGaAs/GaAs quantum well structures. Observation of the laser scatter by the LO phonon as described earlier indicates that the signal-to-noise figure of merit is probably in the range needed to observe hot electron photoluminescence. Therefore, there are several other possibilities for the lack of data. First and foremost is insufficient doping of the bulk samples. Other concerns include the inability to excite the quantum well sample sufficiently far enough from the zone-center transitions and the dual-computer photon-counting scheme.

The maximum doping concentration of the bulk GaAs samples studied was $1.2 \times 10^{14} \text{ cm}^{-3}$ carbon acceptors. It is possible that this concentration provided too few recombination sites for electrons and, therefore, the probability of observing a hot-electron transition decreased to the point it could not be resolved from the noise. As stated in Section A.1, previous experiments used samples with doping concentrations at least one and up to five orders of magnitude higher than these.

For the InGaAs/GaAs quantum well sample where the first quantized heavy hole and light hole energy levels were separated by 27.3 meV (at low temperatures), this complex band structure makes observation of hot electron peaks associated with heavy hole band excitation difficult because the peaks are obscured by the much stronger light

hole transition. If laser excitation energy is increased sufficiently to blue-shift weak hot electron signals from the stationary and stronger quantum state transitions, the GaAs barrier layers begin to be excited as well. With absorption occurring in multiple regions, and the ability for electrons to migrate from the GaAs barrier into the InGaAs well regions, multiple band-to-band transitions are allowed and the probability of isolating hot electron transitions is almost zero.

With independent computers controlling the movement of the monochromator gratings and the triggering of the photon count, averaging occurred since both computers could not remain synchronized. Furthermore, the movement of the grating, since it was controlled by the same source which supplied the high voltage to the PMT, could have added noise to the photon count. It is therefore necessary for the dual-computer scheme to be replaced with single computer control and collection. Through the use of vendor-supplied equipment for signal collection and interpretation (photon counting), the signal would be free from the effects of averaging, as well as any electronic noise associated with a second system. An improved detector should also be included in this photon counting equipment. This detector requires an increased detectivity than that of the S1 detector used for the long wavelength experiments, and will therefore yield lower noise currents and increased signal to noise ratios.

BIBLIOGRAPHY

1. Adachi, Sadeo. Physical Properties of III-V Semiconductor Compounds. New York: John Wiley & Sons, Inc., 1992.
2. Fasol, G. and H.P. Hughes, Physical Review B, **33(4)**: 2953-2956 (February 1986).
3. Goldys, E.M., H.Y. Zuo, M.R. Phillips, C.M. Contessa, M.R. Vaughan, and T.L. Tansley, Journal of Electronic Materials, **26(8)**: 922-927 (August 1997).
4. Kimball, G. E., Journal of Chemical Physics, **3**: 560 (1935).
5. Loehr, J.P., Y.C. Chen, D. Biswas, P. Bhattacharya, and J. Singh, Applied Physics Letters, **57**: 180-182 (1990).
6. Madelung, O. Semiconductors. Group IV Elements and III-V Compounds. New York: Springer-Verlag, 1991.
7. McKelvey, John P. Solid State Physics. Malabar FL: Krieger Publishing Company, 1993.
8. Pankove, Jacques I. Optical Processes in Semiconductors. New York: Dover Publications, Inc., 1971.
9. Rebane, K. and P. Saari, Solid State Communications, **7**: 887 (1969).
10. Reithmaier, J.P., R. Hoger, H. Reichert, A. Heberle, G. Abstreiter, and G. Weimann, Applied Physics Letters, **56**: 536 (1990).
11. Saleh, Bahaa E. A. and Malvin Carl Teich. Fundamentals of Photonics. New York: John Wiley & Sons, Inc., 1991.
12. Singh, J., in Properties of Lattice-Matched and Strained Indium Gallium Arsenide, edited by Pallab Bhattacharya. London: INSPEC, 1993.
13. Ulbrich, R.G., J.A. Kash, and J.C. Tsang, Physical Review Letters, **62(8)**: 949-952 (February 1989).
14. Varshni, Y.P., Physica, **34**: 149 (1967).
15. Yariv, Amnon. Quantum Electronics, Third Edition. New York: John Wiley & Sons, Inc., 1989.
16. Zachau, M., J.A. Kash, and W.T. Masselink, Physical Review B, **44(3)**: 4048-4051 (August 1991).
17. Zakharchenya, B.P., D.N. Mirlin, V.I. Perel, and I.I. Reshina, Soviet Physics-Uspokhi, **25(3)**: 143-166 (March 1982).

REPORT DOCUMENTATION PAGE

*Form Approved
OMB No. 074-0188*

The public reporting burden for this collection of information is estimated to average 1 hour per response, including the time for reviewing instructions, searching existing data sources, gathering and maintaining the data needed, and completing and reviewing the collection of information. Send comments regarding this burden estimate or any other aspect of the collection of information, including suggestions for reducing this burden to Department of Defense, Washington Headquarters Services, Directorate for Information Operations and Reports (0704-0188), 1215 Jefferson Davis Highway, Suite 1204, Arlington, VA 22202-4302. Respondents should be aware that notwithstanding any other provision of law, no person shall be subject to a penalty for failing to comply with a collection of information if it does not display a currently valid OMB control number.

PLEASE DO NOT RETURN YOUR FORM TO THE ABOVE ADDRESS.

| | | | | | | |
|---|--------------|--------------|--|----------------------------|--|--|
| 1. REPORT DATE (DD-MM-YYYY) 03-09-2001 | | | 2. REPORT TYPE Master's Thesis | | 3. DATES COVERED (From - To) Jun 2000 - Mar 2001 | |
| 4. TITLE AND SUBTITLE PHOTOLUMINESCENCE OF SINGLE QUANTUM WELL STRUCTURES IN GALLIUM ARSENIDE | | | | | 5a. CONTRACT NUMBER | |
| | | | | | 5b. GRANT NUMBER SN-AFIT-00-05 | |
| | | | | | 5c. PROGRAM ELEMENT NUMBER | |
| 6. AUTHOR(S) Bartholomew, Christian A., Captain, USAF | | | | | 5d. PROJECT NUMBER ENR 01-414 | |
| | | | | | 5e. TASK NUMBER | |
| | | | | | 5f. WORK UNIT NUMBER | |
| 7. PERFORMING ORGANIZATION NAMES(S) AND ADDRESS(S) Air Force Institute of Technology Graduate School of Engineering and Management (AFIT/EN) 2950 P Street, Building 640 WPAFB OH 45433-7765 | | | | | 8. PERFORMING ORGANIZATION REPORT NUMBER AFIT/GEO/ENP/01M-01 | |
| 9. SPONSORING/MONITORING AGENCY NAME(S) AND ADDRESS(ES) DAGSI Attn: Dr. Frank Moore 3155 Research Boulevard, Suite 205 Kettering, Ohio 45420 Comm: (937) 781-4000 | | | | | 10. SPONSOR/MONITOR'S ACRONYM(S) | |
| | | | | | 11. SPONSOR/MONITOR'S REPORT NUMBER(S) | |
| 12. DISTRIBUTION/AVAILABILITY STATEMENT APPROVED FOR PUBLIC RELEASE; DISTRIBUTION UNLIMITED. | | | | | | |
| 13. SUPPLEMENTARY NOTES | | | | | | |
| 14. ABSTRACT The continued development of state-of-the-art semiconductor technologies and devices by the United States Air Force and the Department of Defense requires accurate and efficient techniques to evaluate and model these new materials. Of particular interest to the Air Force are quantum well structures which can be used for small-scale laser sources in fly-by-light applications, as efficient infrared countermeasures to heat-seeking missiles, or as advanced seekers in optically guided missiles. This thesis provides the initial experimental procedures and data necessary to begin producing accurate yet robust models. Although carrier effective masses could not be evaluated using hot-electron photoluminescence, photoluminescence excitation and temperature studies were conducted to determine the effects of strain and impurities on band structure in quantum structures. Beryllium-doped indium gallium arsenide (InGaAs:Be) quantum wells, compressively strained to lattice-match gallium arsenide, were studied, and parameters for strained energy gap, heavy hole-light hole split, and acceptor binding energy were evaluated. With the carrier effective masses fixed at accepted values, strain produced a 1.2715 eV energy gap within the well and a heavy hole-light hole split of 23.2 meV. Finally, the beryllium binding energy was found to be 22.1 meV measured above the highest valence band (first quantized heavy hole band) at 300 K. | | | | | | |
| 15. SUBJECT TERMS Photoluminescence; Quantum Well; Gallium Arsenide; Indium Gallium Arsenide; Hot Electron Photoluminescence; Strain; Finite Potential Well Model; Beryllium Binding Energy | | | | | | |
| 16. SECURITY CLASSIFICATION OF: | | | 17. LIMITATION OF ABSTRACT | 18. NUMBER OF PAGES | 19a. NAME OF RESPONSIBLE PERSON | |
| a. REPOR T | b. ABSTR ACT | c. THIS PAGE | | | Lt Col M. A. Marciniak, ENP | |
| U | U | U | UU | 76 | 19b. TELEPHONE NUMBER (Include area code) (937) 255-3636, ext 4529 | |

Standard Form 298 (Rev. 8-98)
Prescribed by ANSI Std. Z39-18

*Form Approved
OMB No. 074-0188*